Monthly Notices of the ROYAL ASTRONOMICAL SOCIETY

MNRAS **458,** 394–409 (2016) doi:10.1093/mnras/stw280
Advance Access publication 2016 February 5

The void galaxy survey: Star formation properties

B. Beygu,[1,2★] K. Kreckel,[3] J. M. van der Hulst,[1] T. H Jarrett,[4] R. Peletier,[1] R. van de Weygaert,[1] J. H. van Gorkom[5] and M. A. Aragon-Calvo[6]

[1]*Kapteyn Astronomical Institute, University of Groningen, PO Box 800, NL-9700 AV Groningen, the Netherlands*
[2]*Physics and Centre for Space Research, North-West University, Potchefstroom, South Africa*
[3]*Max Planck Institute for Astronomy, Königstuhl 17, D-69117 Heidelberg, Germany*
[4]*Astronomy Department, University of Cape Town, Rondebosch 7700, Cape Town, South Africa*
[5]*Department of Astronomy, Columbia University, Mail Code 5246, 550 West 120th Street, New York, NY 10027, USA*
[6]*University of California, Riverside, 900 University Ave, Riverside, CA 92521, USA*

Accepted 2016 February 1. Received 2016 February 1; in original form 2015 December 18

ABSTRACT

We study the star formation properties of 59 void galaxies as part of the Void Galaxy Survey (VGS). Current star formation rates are derived from H α and recent star formation rates from near-UV imaging. In addition, infrared 3.4, 4.6, 12 and 22 μm *Wide-field Infrared Survey Explorer* emission is used as star formation and mass indicator. Infrared and optical colours show that the VGS sample displays a wide range of dust and metallicity properties. We combine these measurements with stellar and H I masses to measure the specific SFRs (SFR/M_*) and star formation efficiencies (SFR/$M_{\rm H\,I}$). We compare the star formation properties of our sample with galaxies in the more moderate density regions of the cosmic web, 'the field'. We find that specific SFRs of the VGS galaxies as a function of stellar and H I mass are similar to those of the galaxies in these field regions. Their SFR α is slightly elevated than the galaxies in the field for a given total H I mass. In the global star formation picture presented by Kennicutt–Schmidt, VGS galaxies fall into the regime of low average star formation and correspondingly low H I surface density. Their mean SFR $\alpha/M_{\rm H\,I}$ and SFR α/M_* are of the order of $10^{-9.9}$ yr^{-1}. We conclude that while the large-scale underdense environment must play some role in galaxy formation and growth through accretion, we find that even with respect to other galaxies in the more mildly underdense regions, the increase in star formation rate is only marginal.

Key words: galaxies: formation – galaxies: star formation – galaxies: structure – large-scale structure of Universe.

1 INTRODUCTION

Voids are prominent features of the cosmic web (van de Weygaert & Platen 2011). Formed from primordial underdensities they now occupy a major fraction of the volume of the Universe, surrounded by denser filaments, walls and sheets. They are the most underdense regions in the universe and are the most pristine environments where galaxy evolution will have progressed slowly, without the dominant and complex influence of the environment. Voids therefore are extremely well suited for assessing the role of the environment in galaxy evolution, as here the galaxies are expected not to be affected by the complex processes that modify galaxies in high-density environments. The void environment covers the lowest density environments found in the universe, though some voids do approach similar (and still low) densities as found in tenuous filaments and walls (Cautun et al. 2014). These authors investigate the dark matter halo distribution in the various cosmic web components and demonstrate that in voids very few dark matter haloes more massive than 10^{11} M$_\odot$ exist, confirming the idea that high stellar mass objects are rarely expected in these environments.

In order to get a good picture of galaxies in voids the Void Galaxy Survey (VGS) was designed, a multiwavelength study of ∼ 60 galaxies in geometrically defined voids (Stanonik et al. 2009; Kreckel et al. 2011, 2012; van de Weygaert et al. 2011). Previous papers have focused on the H I properties of galaxies in voids and found that the voids contain a population of galaxies that are relatively H I rich of which many present evidence for ongoing gas accretion, interactions with small companions and filamentary alignments (Kreckel et al. 2011, 2012; Beygu et al. 2013). Void galaxies in general have small stellar masses ($\leq 3 \times 10^{10}$ M$_\odot$). This is consistent with previous studies analysing the optical properties of void galaxies. These show that void galaxies are in general small, star-forming blue galaxies and have late morphological types (Szomoru et al. 1996b; Kuhn, Hopp & Elsaesser 1997; Popescu, Hopp & Elsaesser 1997; Grogin & Geller 1999, 2000;

★E-mail: burcu.beygu@nwu.ac.za

Karachentseva, Karachentsev & Richter 1999; Rojas et al. 2004, 2005; Ceccarelli et al. 2006; Patiri et al. 2006a,b; Tikhonov & Karachentsev 2006; Wegner & Grogin 2008; Kreckel et al. 2011, 2012; Moorman et al. 2014, 2015). Conclusions on the role of void environment relative to the field, however, are not clear. Patiri et al. (2006b), using the Sloan Digital Sky Survey Data Release 4 (SDSS DR4) data, show that void galaxies have the same specific star formation rates (S_SFRs) at a fixed colour as their comparison sample of field galaxies. Similarly Penny et al. (2015) examined the properties of void galaxies in the Galaxy and Mass Assembly (GAMA; Driver et al. 2011) survey. They found that void galaxies with stellar mass $M_* > 5 \times 10^9\,M_\odot$ have ceased forming stars and their infrared colour distribution show a wide range of star formation activity. Rojas et al. (2004, 2005), using equivalent widths of Hα, [O II], [N II], Hβ and [O III] from SDSS DR4, argued that void galaxies have similar star formation rates as field galaxies[1] but since they have smaller stellar masses, their S_SFRs are expected to be higher than field galaxies. Ricciardelli et al. (2014) reported that void galaxies appear to form stars more efficiently then galaxies living in the void shells and the general galaxy population based on their sample form the SDSS DR7. They also find that the star formation rate is insensitive to the environment for their sample when only the star-forming galaxies are considered. Moorman et al. (2016), however, found contradicting results. For a subset sample of optically selected galaxies from the SDSS DR8 with H I detection they found that the S_SFR did not vary systematically with large-scale environment. They also did not find any environmental dependence for the star formation rate per unit H I mass. They discuss in detail that the difference between the results of Ricciardelli et al. (2014) and theirs arises from the different definition of a void. On the other hand, Grogin & Geller (2000) investigated the Hα equivalent widths of void galaxies selected from the 2dF. They found indications that void galaxies with companions to have more elevated star formation rates than comparable field galaxies, while the star formation rate of void galaxies without nearby companions varies little over the entire density range. A study of nearby cosmic voids within a distance of 40 Mpc, by Elyiv et al. (2013), found 48 late-type dwarf galaxies, with a median star formation rate per luminosity of $\sim 10^{-10}\,M_\odot\,yr^{-1}L_\odot^{-1}$. Furthermore, physical properties of 26 emission line galaxies in the Bootes Void have been investigated by Cruzen et al. (2002). They extended the sample used in the Hα imaging of the 12 Bootes Void galaxies investigated by Peimbert & Torres-Peimbert (1992), and spectra of the 10 Bootes void galaxies studied by Weistrop et al. (1995). They did not include, however, additional Bootes Void galaxies reported by Szomoru, van Gorkom & Gregg (1996a), into their sample. By using equivalent widths of Hα+[N II], and line ratios between [O III], Hβ and [S II], Cruzen et al. (2002) identified two extreme starbursts and 13 galaxies with elevated rates of star formation out of 26 galaxies.

In most of the previous studies (Rojas et al. 2004, 2005; Hoyle, Vogeley & Pan 2012; Ricciardelli et al. 2014; Moorman et al. 2016), star formation rate measurements were mostly based on aperture corrected spectra of large survey data without any information about the star formation distribution throughout the galaxy. They are missing the combination of Hα, UV, infrared and 21-cm neutral hydrogen imaging data through which star formation efficiencies, current and recent star formation properties of void galaxies can be directly measured and emission morphologies can be clearly investigated. Although, studies of Peimbert & Torres-Peimbert (1992), Weistrop et al. (1995), Szomoru et al. (1996a) involve individual observations, their sample either suffer from selection effects (since the sample consist of mostly *IRAS* selected galaxies) or lack of completeness.

In this study, we present, for the first time, star formation properties of void galaxies measured from systematic Hα, near-UV (NUV), infrared and 21-cm neutral hydrogen imaging surveys. We assume $H_0 = 70\,km\,s^{-1}\,Mpc^{-1}$.

This study is part of the VGS (Kreckel et al. 2011; van de Weygaert et al. 2011) and targets the galaxies selected for that study (59 targeted galaxies and 18 companions confirmed by either 21-cm neutral hydrogen or optical observations[2]).

2 THE VGS SAMPLE: OBSERVATIONS AND REDUCTION

Galaxies in the VGS have been selected from the SDSS DR7 using purely geometric and topological techniques. The sample was selected on the basis of galaxy density maps produced by the Delaunay Tessellation Field Estimator (DTFE, Schaap & van de Weygaert 2000; van de Weygaert & Schaap 2009) and the subsequent application of the Watershed Void Finder (WVF; Platen, van de Weygaert & Jones 2007). The combination of DTFE maps with WVF detected voids allow us to identify void galaxies from the deepest interior regions of identified voids in the SDSS redshift survey. Our sample has a density contrast, $\delta \equiv \rho_{void}/\rho_u - 1$, of less than -0.5, where ρ_u is the mean density. In Fig. 1, we present two examples displaying two different environments surrounding the voids in which two of the VGS galaxies reside. One (Fig. 1a) is the environment of the polar disc galaxy (VGS_12) mentioned above, and the other (Fig. 1b) is the environment of a flocculent galaxy (VGS_32) sitting in a void that is surrounded by a massive filament.

Our geometrically selected sample consists of small galaxies, with stellar mass less than $3 \times 10^{10}\,M_\odot$. The H I mass range of our sample is between 10^7 and $10^{10}\,M_\odot$ and there redshifts range from 0.02 to 0.03. Most of them are blue star-forming disc galaxies and many of them have companions and extended H I discs, which are often morphologically and kinematically disturbed (Kreckel et al. 2011, 2012). Two objects have been investigated in great detail. One of them is a polar disc galaxy (VGS_12), with an H I disc, about nine times the extent of the stellar disc, rotating with an angle perpendicular to the stellar disc (Stanonik et al. 2009). The second one, VGS_31, is a system of three interacting galaxies forming a filamentary structure inside a void (Beygu et al. 2013).

The VGS galaxies have been observed in the *B* band, Hα, UV, near-IR and in the H I. Narrow band Hα imaging has been obtained using the Hiltner Telescope at the Michigan-Dartmouth-MIT Observatory (MDM). *B*-band imaging has been gathered with the Isaac Newton Telescope (INT) at La Palma using the Wide Field Camera NUV images have been taken with *Galaxy Evolution Explorer* (*GALEX*). Near-infrared (NIR) images have been obtained from the *Wide-field Infrared Survey Explorer* (*WISE*) survey using Jarrett's pipeline (Jarrett et al. 2013) to extract calibrated in the 3.4, 4.6, 12

[1] In their method field galaxies are indicated by the name 'wall galaxies' as defined in Hoyle & Vogeley (2002).

[2] The original sample was meant to contain 60 galaxies. However, one of the galaxies, VGS_28, has been removed from the sample since redshift information from the latest SDSS release was inconsistent with the previous SDSS data releases and placed it well outside void. It was also not detected in H I as redshift is outside the observing band. This reduces the number of targeted galaxies to 59.

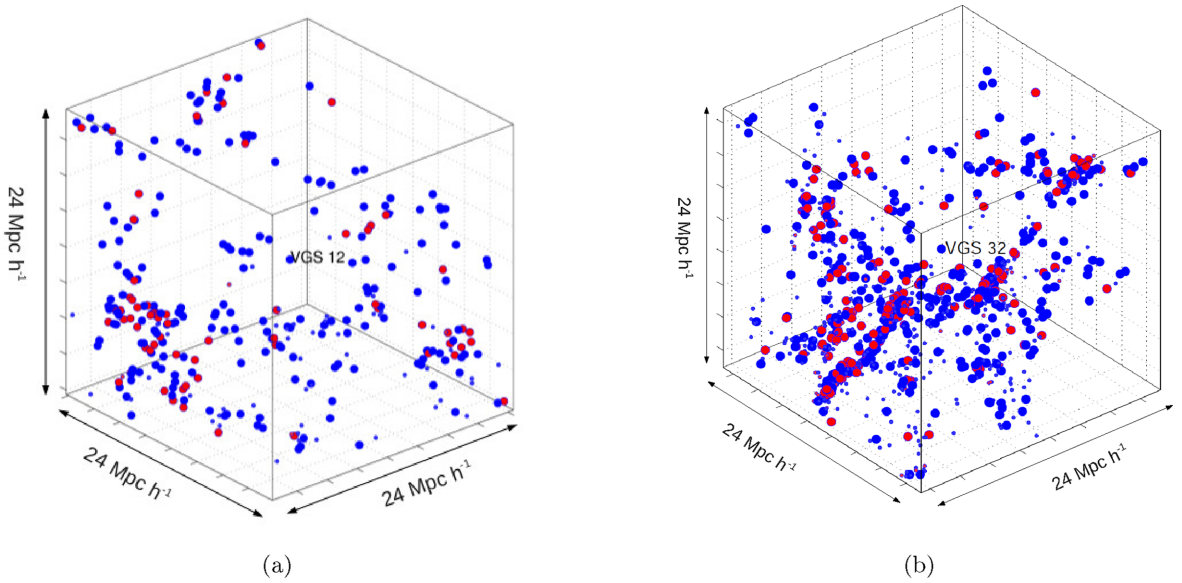

Figure 1. The large-scale structure distribution of galaxies within 24 Mpc h^{-1} in comoving coordinates around VGS_12 (a) and VGS_32 (b). Surrounding galaxies are colour coded by $g - r$ colour, to be red if $g - r > 0.6$ and blue if $g - r \leq 0.6$. The symbol size indicates luminosity, with larger symbols if $M_r < -18$ and smaller symbols if $M_r \geq -18$. M_r is derived from the SDSS DR7 apparent r model magnitudes.

and 22 μm bands. A detailed description of these data sets is given below. In an accompanying paper morphology and colour properties of the VGS galaxies derived from these data will be discussed (Beygu et al. in preparation).

2.1 H I imaging

The VGS galaxies have been observed with the Westerbork Synthesis Radio Telescope (WSRT) (Kreckel et al. 2012) in the maxi-short configuration providing an angular resolution of 19 arcsec × 32 arcsec. We observed 512 channels within a total bandwidth of 10 MHz, giving a Hanning smoothed velocity resolution of 8.6 km s^{-1}. The 36 arcmin full width half-maximum of the WSRT primary beam and the given total bandwidth allowed us to probe a total volume covering ∼ 1.2 Mpc and 1200 km s^{-1} at 85 Mpc. Images for this paper were made with natural weighting to maximize sensitivity and cleaned to a level of 0.5 mJy beam^{-1} ($\sim 1\sigma$), reaching column density sensitivities of 2×10^{19} cm^{-2}. H I detections and masses are given in table 2 in Kreckel et al. (2012) for the full sample of VGS galaxies.

2.2 H α imaging

H α imaging has been obtained with the Echelle CCD in direct mode at the 2.4 m Hiltner Telescope. The redshifted H α filters centred at 6649 and 6693 Å were used (Fig. 2). To have a measure of the continuum, *R*-(Harris) band imaging was performed for each object. The total integration time for H α (1800 s) and for the continuum (360 s) was spread over 3 exposures for the purpose of dithering and for facilitating cosmic ray detection. Spectrophotometric calibration stars were chosen from either Massey et al. (1988) or Oke (1990). 59 VGS galaxies and 8 out of 17 companions have been observed in H α. In total 62 galaxies have been detected.

The datahave been reduced using the standard IRAF[3] procedures for CCD imaging. All the optical images were trimmed and overscanned followed by bias subtraction and flat fielding. All images from each filter were aligned and median combined. Each combined H α and *R*-band image was normalized by the integration time. The mean was calculated for an empty region in each image and the ratio of these means was taken as scaling factor for scaling the continuum image before subtraction from the H α image. The photometric calibration of the final H α images was performed following the steps described in Gavazzi et al. (2006) and references therein. Corrections for the atmospheric extinction and the airmass have been performed in the standard way, where each spectrophotometric calibration star observation has been fitted

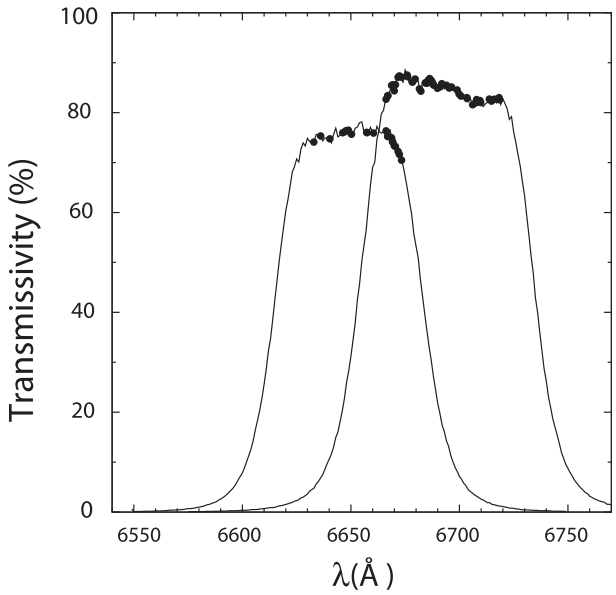

Figure 2. The transmissivity of the H α filters with central wavelengths of 6649 and 6693 Å. Filled circles mark the transmissivity for H α at the redshift of the target galaxies.

[3] http://iraf.noao.edu/

using airmass and instrumental magnitudes to get the atmospheric extinction coefficient. The final Hα images have been created by

$$C_{\rm ON} - nC_{\rm OFF} = C_{\rm NET}, \quad (1)$$

where n is the scaling factor or normalization coefficient, $C_{\rm ON}$ and $C_{\rm OFF}$ are the flux in counts per second for the Hα and continuum filters, respectively, and $C_{\rm NET}$ is the net flux in counts after subtracting the continuum. After checking the mean of flux for the stars in the field, n was improved if necessary.

Flux calibration has been performed using spectrophotometric standard stars, following the basic photometry equation relating magnitude, m and flux, $F_{\rm star}$:

$$m = -2.5\log(F_{\rm star}) + C_{\rm star}. \quad (2)$$

This yields:

$$-2.5\log(F_{\rm star}) = -2.5\log(C_{\rm star}) + m_{\rm ZP} - \kappa sec(z), \quad (3)$$

where $m_{\rm ZP}$ is magnitude zero-point, κ is the atmospheric extinction coefficient, $sec(z)$ is the airmass, $C_{\rm star}$ is the standard star's total counts in an aperture and $F_{\rm star}$ is the flux density of the standard star calculated as

$$F_{\rm star} = \int S(\lambda) R_{\rm ON}(\lambda)\, {\rm d}\lambda, \quad (4)$$

where $S(\lambda)$ is the spectral energy distribution of the standard star and $R_{\rm ON}(\lambda)$ is the transmissivity of the Hα filter as a function of wavelength. Then the total Hα flux, $F({\rm H}\alpha)_0$(contaminated by [N II]) for a galaxy is

$$F({\rm H}\alpha)_0 = 10^{\log\left(\frac{F_{\rm star}}{C_{\rm star}}\right) - 0.4\kappa \sec(z)} \times \frac{C_{\rm NET}}{R_{\rm ON}(z)}, \quad (5)$$

where $R_{\rm ON}(z) = R_{\rm ON}(Filter \times (1+z))$ is the transmissivity of the Hα filter as a function of a galaxy's redshift. Correction for the contamination of the Hα line emission in the continuum filter yields:

$$F({\rm H}\alpha) = {\rm F}({\rm H}\alpha)_0 \times \left[1 + \frac{\int {\rm R_{ON}}(\lambda){\rm d}\lambda}{\int {\rm R_{OFF}}(\lambda){\rm d}\lambda}\right], \quad (6)$$

where $F({\rm H}\alpha)$ is the line corrected flux and $R_{\rm ON}(\lambda)$ and $R_{\rm OFF}(\lambda)$ are the transmissivities of the Hα and the continuum filters, respectively.

The Hα line fluxes measured within the 3 arcsec fibre apertures of the SDSS pipeline compare very well with the Hα fluxes extracted in 3 arcsec apertures from the MDM Hα narrow band images (Fig. 3), thus confirming the calibration. Both Hα flux measurements include a contribution from the [N II] lines.

2.2.1 *Correction for [N II] line contamination*

The contribution of the [N II] line to the observed flux has been estimated using the expression from Kennicutt et al. (2008):

$$\log([{\rm N\,II}]/{\rm H}\alpha) = \begin{cases} (-0.173 \pm 0.007) M_B - (3.903 \pm -0.137) & \text{if } M_B > -21, \\ 0.54 & \text{if } M_B \leq -21, \end{cases}$$

and has been subtracted from the Hα flux. $M_{\rm B}$ has been calculated from the SDSS g magnitudes following Gavazzi et al. (2012).

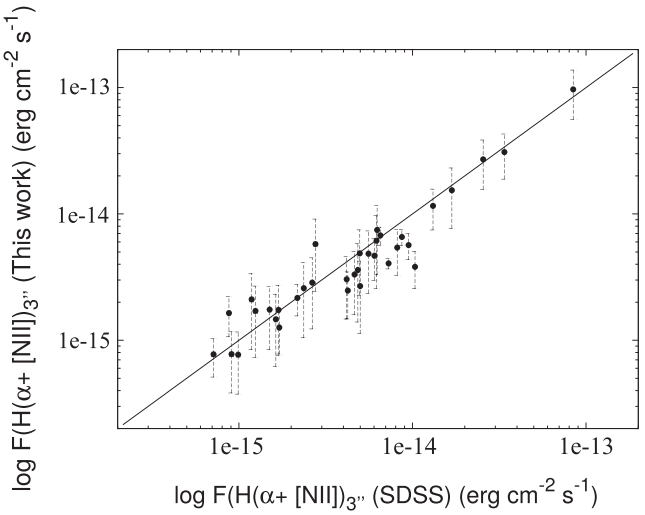

Figure 3. Comparison between the Hα + [N II] fluxes extracted in 3 arcsec aperture from this work and the Hα + [N II] lines given by the MPA/JHU catalogue in 3 arcsec fibre spectrum. The solid line is the identity line. Only the galaxies with high S/N > 3 detection are plotted. Errors on SDSS Hα + [N II] fluxes are significantly small compared to this work, therefore they are not visible in the plot.

2.3 NUV imaging

NUV data have been obtained with *GALEX* satellite, primarily collected under the Guest Investigator program 061 in Cycle 6. Observations have exposure times of $\sim$ 1600 s. The data was calibrated using the standard *GALEX* pipelines. NUV magnitudes ($m_{\rm AB}$) are taken from the *GALEX* pipeline catalogue as measured with a Kron aperture (Kron 1980). The flux density f_υ is given by

$$f_\upsilon[{\rm erg\ s^{-1} cm^{-2} Hz^{-1}}] = 10^{-0.4(m_{\rm AB}+48.6)} \quad (7)$$

59 VGS galaxies and 11 companions have been detected in the NUV.

2.4 Ancillary data: SDSS and *WISE*

In addition to our own observations we also make use of archival data. Before summarizing our observations and data analysis steps, we describe the archival data we used to complement our analysis.

2.4.1 *SDSS photometric and spectroscopic data*

Hα, Hβ, [N II] and [O III] emission line fluxes, 4000 Å break values ($D_n(4000)$),($g-r$) colours and the gas-phase metallicities (12+log(O/H), following Tremonti et al. 2004) of the VGS galaxies have been taken from the MPA/JHU catalogue for SDSS DR7. These have been measured from the SDSS DR7 spectra which cover the central 3 arcsec of each object. Average distance of our sample is $\sim$ 80 Mpc. At this distance 3 arcsec corresponds to a physical scale of 1.6 kpc. Absolute B magnitudes ($M_{\rm B}$) of the VGS galaxies have been calculated using the SDSS g magnitudes, following Gavazzi et al. (2012) and references therein. We used the Hα and Hβ line fluxes to measure Balmer decrements of VGS galaxies as described in Section 3.5.1.

We used [N II] and [O III] line fluxes in order to create a Baldwin, Phillips & Terlevich (BPT) diagram (Fig. 13). For this, only galaxy spectra whose measured line amplitudes are five times the size of the residual noise have been used. Among these galaxies, only one

galaxy spectrum (VGS_24), has been fitted separately using the PPXF (Cappellari & Emsellem 2004) and GANDALF (Sarzi et al. 2006) packages since it is classified as broadline object[4] and the SDSS pipeline has problems with fitting the spectra of these objects.

The MPA/JHU catalogue for SDSS DR7[5] provides stellar mass estimates that are obtained using fits to the *ugriz* photometry following the methods described in Kauffmann et al. (2003) and Salim et al. (2007). In Kreckel et al. (2012), we have adopted the stellar masses given by the MPA/JHU catalogue for the full sample of the VGS galaxies. In this study, we also use the *WISE* [3.4] and [4.6] data to determine the stellar mass of the VGS galaxies in order to be consistent with the stellar mass measurements of the comparison sample for which stellar masses are determined via infrared data. A comparison between stellar masses determined by the *WISE* measurements and the MPA/JHU catalogue is given in Section 4.1.

2.4.2 *WISE data*

WISE 3.4, 4.6, 12 and 22 μm measurements have been retrieved from the *WISE* All-sky source catalogue (Wright et al. 2010). Resolved sources (the *WISE* angular beam is about 6 arcsec) are measured using code and tools developed for the *WISE* photometry pipelines (Jarrett et al. 2011, 2013; Cutri et al. 2012). More details may be found in Cluver et al. (2014).

Of the 59 VGS galaxies, 36 have been detected in 12 μm and 18 have been detected in 22 μm with the *WISE*. We used the following zero magnitude flux densities which correspond to *WISE* bands (W1, W2, W3 and W4) with effective wavelengths 3.35, 4.60, 11.56 and 22.8 μm, respectively: 309.68, 170.66, 29.05 and 7.871 Jy (Wright et al. 2010; Jarrett et al. 2011; Brown, Jarrett & Cluver 2014).

We use the calibrated 12 and 22 μm bands to derive the star formation rates (Jarrett et al. 2013) from warm-dust emission of the galaxies and compare them to SFRα and SFR$_{\rm NUV}$ as described in Section 4.2. We determine stellar mass from 3.4 and 4.6 μm bands according to Cluver et al. (2014, , Section 4.1). The stellar mass data have been used to measure S_SFRs, by normalizing the Hα and UV SFRs by the stellar masses.

3 COMPARISON SAMPLES

For a proper interpretation of our results it is necessary to compare the star formation properties of the VGS galaxies with those of a comparison sample. It is difficult, however, to find such a sample because one needs galaxies which belong to environments that are only moderately denser than the voids and for which reliable data of similar quality is available. In addition, the environment for such a sample should be defined the same way as for the VGS sample. In very general terms 'the field' is everywhere but in void interiors, and more than a several tidal radii away from dense clusters of galaxies. We call these environments 'the field' in this paper, they are the moderate density areas corresponding to the outer boundary regions of voids, the outskirts of filaments and the intermediate wall-like regions in the Cosmic Web (Aragón-Calvo, van de Weygaert & Jones 2010; Cautun et al. 2014). Finding a comparison sample that fulfils these requirements and for which data on the H I, stellar mass and star formation properties, is available is not trivial. Our comparison samples consist of galaxies within the same stellar mass ranges as the VGS galaxies ($M_* < 3 \times 10^{10}$ M$_\odot$). The stellar mass of the comparison samples is derived from infrared measurements of various bands, such as 2.2 μm (*K* band), *WISE* 3.4 μm and *Spitzer* 3.6 μm. To be consistent with our data we made sure that the Hα SFRs of the comparison sample are derived via Hα imaging, not from spectra. They have been selected from three studies as described in the next subsections. One sample is complete and volume limited, the other samples are flux limited, but over a much larger volume. These are subject to similar selection effects as the VGS sample.

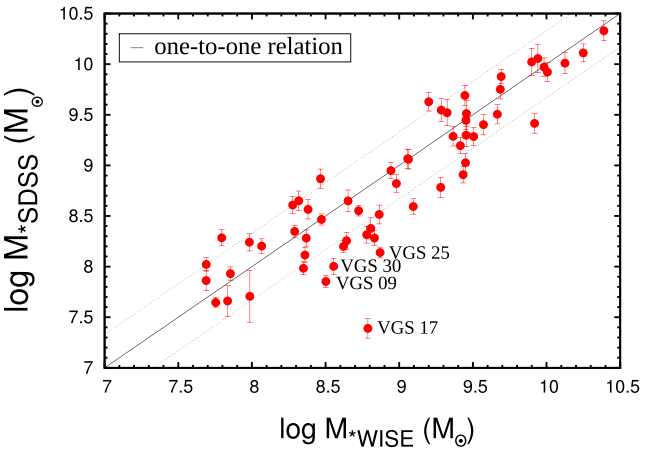

Figure 4. Comparison between the *WISE*-derived and SDSS MPA/JHU stellar mass estimates for the VGS galaxies. Solid black line indicates a one-to-one correspondence while dotted lines are 1σ scatter. Outliers with low signal to noise in *WISE* are labeled.

3.1 A complete sample: local volume field and isolated galaxies

The advantage of a complete, volume limited sample is that it has a full inventory of all galaxies. If the volume is large enough that a range of environments is sampled, then a complete sample offers the additional advantage that it is possible to compare the properties of galaxies in the different environments. Such a complete sample has been put together for the Local Volume (LV) by Karachentsev, Makarov & Kaisina (2013, ; also see Karachentsev & Kaisina 2013). The LV galaxy catalogue includes 873 galaxies that are within 11 Mpc around the Milky Way or have corrected radial velocities $v_{\rm LG} < 600$ km s^{-1}. The sample consist of many dwarf galaxies with $M_{\rm B}$ between -10 and -15 mag. Karachentsev et al. (2013) define a parameter called 'the tidal index Θ', that they use as a quantitative indicator for the density of a galaxy's environment. Using their classification, we have selected the galaxies which are either in the field of the local volume and/or isolated. Besides the Hα star formation information, H I and stellar mass and $M_{\rm B}$ data are taken from their catalogue and atlas of local volume galaxies. Stellar masses of these LV galaxies have been derived from their *K*-band luminosities. Within this LV galaxy catalogue, we have selected 115 local volume field and 61 local volume isolated galaxies which are at the same stellar mass range as the VGS galaxies.

3.2 Flux limited samples: ALFALFA and JCMT NGLS

The disadvantage of the volume limited LV sample is that is does not have many objects in the high stellar and H I mass range. To

[4] In the SDSS spectroscopic catalogue if any galaxies or quasars have lines detected at the 10σ level with $\sigma > 200$ km s^{-1} at the 5σ level, the indication 'BROADLINE' is appended to their subclass.

[5] The MPA-JHU catalogue is publicly available and may be downloaded at http://www.mpa-garching.mpg.de/SDSS/DR7/archive.

sample those one has to resort to flux limited samples which cover a much larger volume, but are incomplete in the low-mass range. Such samples do have selection effects, but these are not dissimilar from those of the VGS sample, which is also biased by the flux limit for spectroscopic data in SDSS.

One flux limited comparison sample has been selected from the catalogue presented in Gavazzi et al. (2012). This catalogue results from an Hα imaging survey of galaxies drawn from the Arecibo Legacy Fast ALFA (ALFALFA) blind H I survey. It consists of ∼400 galaxies in the Local Supercluster and Virgo cluster. A subsequent study (Gavazzi et al. 2013) presents the star formation properties of galaxies in the Virgo cluster and galaxies located in a large area around the Virgo cluster.

Using the latter, we have created a comparison sample (ALFALFA low density) to compare, in particular, with the star formation properties of the VGS galaxies. Out of the 235 galaxies provided by Gavazzi et al. (2012) we have selected galaxies which reside in underdense environments. For the selection, we used the local environment measures based on volume limited samples of ALFALFA galaxies selected from the SDSS spectroscopic survey (Jones et al. 2016). The volume limited sample covers the distance range 500-15 500 km s^{-1}/H_0 and includes all galaxies brighter than $M_r = -18.9$ mag. Two kinds of environment measures are calculated based on this volume limited sample; fixed aperture and nearest neighbour distance. In this study, we adopt the environment measure based on the latter where the nearest neighbour density for each ALFALFA galaxy is calculated based on the projected distance to the third closest galaxy in the reference SDSS catalogue. Using this nearest neighbour statistics we selected the galaxies which have 3rd nearest neighbour density smaller than the mean density of −0.5 of the whole volume limited sample (see fig. 3 in Jones et al. 2016).

After this we compare the entries with the *Spitzer* Survey of Stellar Structure in Galaxies (S^{4}G) catalogue (Sheth et al. 2010; Querejeta et al. 2015). S^{4}G is a volume, magnitude and size limited ($d < 40$ Mpc, $|b| > 30°$, $m_B < 15.5$ and $D_{25} > 1$ arcmin) survey of 2331 galaxies using the 3.6 and 4.5 μm fluxes from the Infrared Array Camera to derive stellar masses. The final ALFALFA comparison sample consists of 33 galaxies. We use the SFRs and H I masses of these galaxies as given in Gavazzi et al. (2012).

Another comparison sample was drawn from the James Clerk Maxwell Telescope (JCMT) NGLS (Nearby Galaxies Legacy Survey), a project geared to imaging 156 nearby galaxies in CO and the NIR (Wilson et al. 2009). Sánchez-Gallego et al. (2012) have defined 72 H I flux limited field galaxies as part of this survey. Among these, 43 have similar stellar mass as our VGS sample and these are added to our comparison sample. Their stellar masses have been taken from S^{4}G catalogue, the same way as done for the ALFALFA sample.

4 DERIVED PROPERTIES

4.1 Stellar masses

There are different methods to determine stellar masses. All are based on observations in different bands in the optical and the IR, and involve an estimate of the spectral energy distribution coupled to stellar population models. For this study it is important that the stellar masses for both the VGS sample and the comparison samples have been determined with the same method to avoid systematic effects. For this study, we adopt to determine stellar masses using the *WISE* [3.4]–[4.6] colour and the mass-to-light ratio relation of 3.4 μm luminosity given in Cluver et al. (2014).[6] The assumption is that the infrared 3.4 and 3.6 μm emission from galaxies mainly traces the old star population and has been shown to be an effective measure of galaxy stellar mass (Jarrett et al. 2013; Cluver et al. 2014; Meidt et al. 2014). For low redshift sources this gives:

$$\log_{10} M_*/L_{3.4} = -2.54 \times ([3.4] - [4.6]) - 0.17, \quad (8)$$

where $L_{3.4}(\mathrm{L}_\odot) = 10^{-0.4(\mathrm{M}-\mathrm{M}_\odot)}$, M is the absolute magnitude of the source in 3.4 μm and $\mathrm{M}_\odot = 3.24$ (Jarrett et al. 2013).

In Fig. 4, we compare our stellar mass estimates derived using *WISE* data to those of SDSS MPA/JHU catalogue for SDSS DR7 which we used in our earlier VGS studies (Kreckel et al. 2012, 2013). The mass estimates agree with a standard deviation of a factor of ∼ 2. Both SDSS and *WISE* stellar mass estimates agree on the upper limit of stellar mass of $M_* < 3 \times 10^{10}$ $\mathrm{M}_\odot$ Outliers such as VGS_09, VGS_17, VGS_25 and VGS_30 have low signal to noise (<3), notably in [3.6]–[4.6] colour and are not included into the S_SFR calculations.

4.2 Star formation rates

Star formation rates can be estimated from Hα fluxes and from NUV fluxes. Both require a correction for extinction. An alternative way to determine star formation rates is to use mid IR data, in particular emission at 12 and 22 μm (Jarrett et al. 2013). Below we describe the various methods and compare them.

4.2.1 The Hα star formation rate

Before calculating star formation rates one needs to correct the Hα fluxes for extinction. A well-known method is to use the Balmer decrement from spectroscopic data. We checked the Balmer decrements using the Hα/Hβ from the MPA-JHU DR7 catalogue for the SDSS 3 arcsec spectra. We selected the good S/N spectra and we made sure that the SDSS fibre was at the correct place, by comparing the Hα flux with our own Hα images. Of the 75 VGS galaxies including companions, 46 of them there are 14 VGS galaxies whose optical and/or Hα disc sizes are comparable to the SDSS 3 arcsec fibre aperture.

For these galaxies SDSS spectra are representative for the whole galaxy disc and therefore the measured Balmer decrements can be safely used to correct the internal extinction. If the Balmer decrement values are higher than the theoretical prediction, i.e. $\simeq 2.88$, for $T \sim 10^4$ K and an electron density of $n_e < 10^6$ cm^{-3} (Calzetti 2001), we used its value to estimate the attenuation. Our sample has Balmer decrement values ranging from 2.9 to 6.1, for the objects with Hα/H$\beta > 2.88$. For the rest of the galaxies, we also looked at the 22 μm detections from the *WISE* and the 4000 Å break ($D_n(4000)$) measurements from the SDSS spectra. If a galaxy has an Hα disc much larger than the 3 arcsec aperture, a Balmer decrement value higher than 2.88 and is detected in 22 μ, then we used the Balmer decrement value to estimate the extinction. This correction assumes that the Hα/Hβ is the same throughout the entire Hα emission region. If it is neither detected in 22 μ nor has a good quality SDSS spectra, then we used the NUV extinction (A_{NUV}), derived using the $D_n(4000)$ parameter and k corrected $^{0.1}$(NUV − r) colour as described in the next subsection, to estimate the Hα extinction ($A\,\alpha$). For these cases, we consider $D_n(4000)$

[6] *WISE* masses are calibrated using GAMA-derived masses, which are essentially SDSS colours.

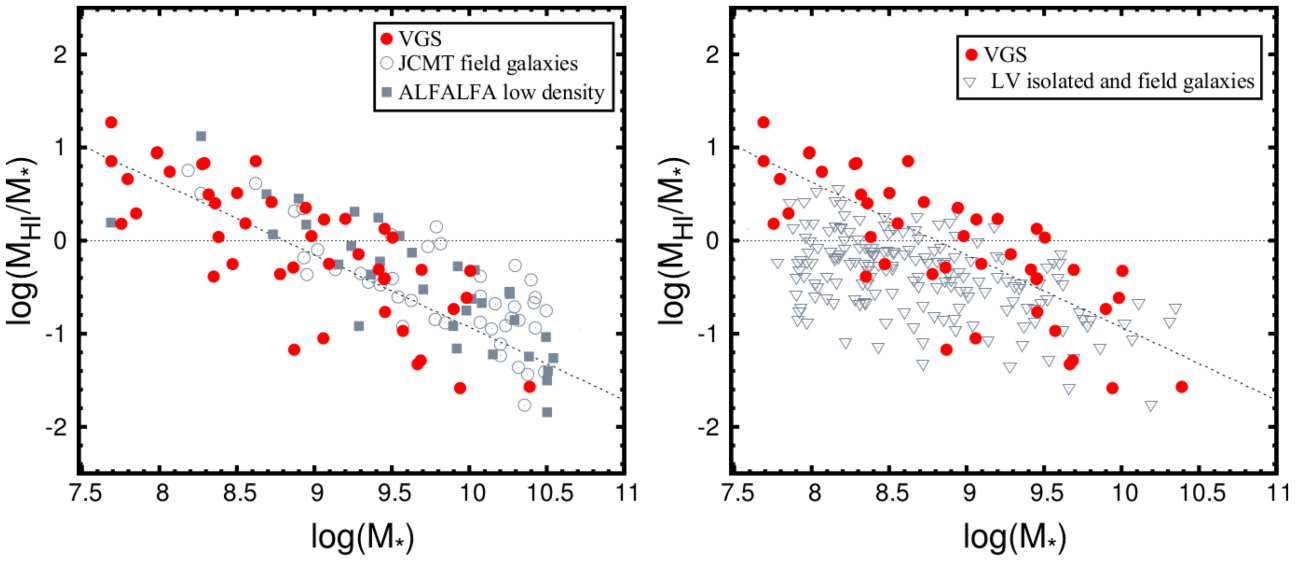

Figure 5. The $M_{\rm H\,I}$-to-M_* ratio for the VGS galaxies and galaxies from intermediate density environment as a function of stellar mass. The comparison samples span the same magnitude range as the VGS galaxies. VGS galaxies are presented as filled red circles. The dashed line is the best fit ($\log(\rm M_{H\,I}/M_*) = -0.78 \times \log(\rm M_*) + 6.87$) to the VGS galaxies detected in H I. The dotted line indicates equal H I mass to stellar mass. The comparison sample consist of ALFALFA galaxies of low-density environments taken from Gavazzi et al. (2012), field galaxies (JCMT field galaxies) presented in Sánchez-Gallego et al. (2012) (a), and local volume (LV) isolated and field galaxies defined in Karachentsev & Kaisin (2010) and Karachentsev & Kaisina (2013) (b), LV galaxies are less H I rich for the given M_* range than the VGS, ALFALFA and the JCMT field galaxies.

measured in the 3 arcsec fibre to be more representative for the entire galaxy than the Balmer decrement value.

In order to calculate the intrinsic H α flux we followed the recipes in Calzetti et al. (2000) and Domínguez et al. (2013) which give:

$$I(H_\lambda) = F(H_\lambda) \times 10^{(0.4 \times A_\lambda)}, \quad (9)$$

where $I(H_\lambda)$ and $F(H_\lambda)$, are the intrinsic and the observed flux densities, respectively, and $\rm A_\lambda$ is the attenuation at wavelength λ (in this case it is the attenuation in H α ($A\,\alpha$)). We have derived $A\,\alpha$ from the Balmer decrement (f_α/f_β) as stated in Lee et al. (2009b) or from $\rm D_n(4000)$ as outlined above

$$A_\alpha = 5.91 \times \log\left(\frac{f_\alpha}{f_\beta}\right) - 2.7. \quad (10)$$

Star formation rates have been calculated from the H α emission following the conversion of Kennicutt et al. (2008):

$$\rm SFR\,\alpha\ [M_\odot\ yr|^{-1}] = 5.4 \times 10^{-42} \times L(H\,\alpha), \quad (11)$$

where L(H α) is the luminosity, calculated as

$$L(\rm H\,\alpha) = 4\pi\ d^2 (3.086 \times 10^{24})^2\ I(H\,\alpha), \quad (12)$$

where d the distance to the galaxy in Mpc derived using spectral redshifts from SDSS and I(H α) is the extinction corrected H α flux. Our results and overall trends do not depend significantly on whether the SFRs are corrected for extinction or not.

4.2.2 *The NUV star formation rate*

In order to estimate the star formation rate from NUV, we first need to estimate the extinction $A_{\rm NUV}$ in the NUV. This can be estimated using two methods. In the first method, $A_{\rm NUV}$ is calculated using $E(B-V)_{\rm gas}$. This has been derived in the previous subsection for the objects where the Balmer decrement is representative for the whole H α emitting disc. Following Calzetti (2001) and Kreckel et al. (2013), this yields:

$$A_{\rm NUV} = 8.189 \times E(B-V)_{\rm stars}, \quad (13)$$

$$E(B-V)_{\rm stars} = 0.47 \times E(B-V)_{\rm gas}, \quad (14)$$

where $E(B-V)_{\rm star}$ is the colour excess of the stellar continuum.

The colour excess of the nebular emission lines, $E(B-V)_{\rm gas}$, has been calculated using $A\,\alpha$ according to Cardelli, Clayton & Mathis (1989),

$$E(B-V)_{\rm gas} = \frac{A\,\alpha}{2.532}. \quad (15)$$

We have used $E(B-V)_{\rm gas}$ to derive extinctions for the NUV ($A_{\rm NUV}$), for the cases where we consider the Balmer decrement to be representative for the whole H α emitting disc.

In the second method, we use $\rm D_n(4000)$ and the (NUV−r) colour to calculate $A_{\rm NUV}$. SDSS r magnitudes are corrected for galactic extinction, $\rm A_\lambda$, using the catalogued extinctions (Schlegel, Finkbeiner & Davis 1998). For the NUV magnitudes, we calculated the galactic extinction following Wyder et al. (2007), who adopted $A_{\rm r}/\rm E(B-V) = 2.751$ and $A_{\rm NUV}/\rm E(B-V) = 8.189$, giving $A_{\rm NUV} = 2.9807 A_{\rm r}$.

The 4000 Å break, $\rm D_n(4000)$ as defined in Balogh et al. (1999), is taken from the MPA/JHU catalogue. If $\rm D_n(4000) > 1.7$, we adopt $A_{\rm NUV} = 0$ (the only case is VGS_05). If $\rm D_n(4000) < 1.7$ then we follow Calzetti et al. (2000) and use $A_{\rm NUV} = 0.81 A_{\rm IRX}$. $A_{\rm IRX}$ is defined in Johnson et al. (2007) as:

$$A_{\rm IRX} = 1.25 - 1.33x + 1.19y - 1.02xy, \quad (16)$$

where $x = \rm D_n(4000) - 1.25$ and $y = {}^{0.1}(\rm NUV - r) - 2$. We calculate the k-corrected NUV and r-band magnitudes band shifted to $z = 0.1$, ${}^{0.1}(\rm NUV - r)$, using the KCORRECT (v4.1.4) package using the method of Blanton & Roweis (2007).

The SFR_{NUV} has been calculated from the *GALEX* NUV luminosities, corrected for internal dust attenuation following the method outlined in Schiminovich et al. (2010).

$$SFR_{UV}[M_\odot\ yr^{-1}] = \frac{L_{UV}\, f_{UV}(young) 10^{0.4 A_{UV}}}{\eta_{UV}}, \quad (17)$$

where L_{UV} is the luminosity in erg $s^{-1}Hz^{-1}$, f_{UV}(young) is the fraction of light that originates in young stellar populations, η_{UV} is the conversion factor between UV luminosity and recent-past-averaged star formation rate and A_{UV} is the dust attenuation. Following Schiminovich et al. (2010), we assumed $f_{UV}(young) = 1$ and $\eta_{UV} = 10^{28.165}$.

Most of the companion galaxies do not have spectra in SDSS and thus do not have a measured value for $D_n(4000)$. This is problematic, as the dust attenuation in the NUV is significant and can decrease the observed SFR by up to an order of magnitude. For galaxies without a measured $D_n(4000)$, we assume a fixed value of 1.25, which is the median value from Johnson et al. (2007) and appears appropriate for our stellar mass range (see fig. 1; Kauffmann et al. 2003). A choice of $D_n(4000)$=1.0 would increase the SFR by 10-30 per cent.

4.2.3 *The mid-IR star formation rate*

Star formation rates from the mid-IR fluxes at 12 and 22 μm (SFR_{12} and SFR_{22}, respectively) have been calculated following the conversion of Jarrett et al. (2013),

$$SFR_{12}(\pm 0.28)(M_\odot\ yr^{-1}) = 4.91(\pm 0.39) \times 10^{-10} \nu L_{12}(L_\odot), \quad (18)$$

$$SFR_{22}(\pm 0.04)(M_\odot\ yr^{-1}) = 7.50(\pm 0.07) \times 10^{-10} \nu L_{22}(L_\odot), \quad (19)$$

where νL_{12} and νL_{22} are the luminosity densities for the 12 and 22 μm and $L_\odot$ is the total solar luminosity equal to 3.839×10^{33} erg s^{-1}.

5 RESULTS

By combining the star formation rates with H I and stellar masses, we can examine the general star formation properties, S_SFRs and star formation efficiencies of our void galaxy sample and compare these with those of field galaxies. Our results, showing the basic scaling relations, are presented in the following subsections. We examine the star formation, stellar and H I properties of the VGS galaxies and compare these with the same properties of objects in the comparison samples.

5.1 H I and stellar masses

In Fig. 5, we show the M_{H_I}-to-M_* ratios (gas fractions) as a function of M_* of the VGS galaxies and the galaxies in the comparison samples. For a clear presentation, we separate the ALFALFA and JCMT samples (Fig. 5a) from the LV galaxy sample (Fig. 5b). In both plots, we show the best fit, $\log(M_{H_I}/M_*) = -0.78 \times \log(M_*) + 6.87$, to the VGS galaxies to highlight the distribution of the comparison sample with respect to the VGS galaxies.

The VGS galaxies are very similar in gas content to the ALFALFA/JCMT galaxies. In the lower stellar mass range ($M_* < 10^9$) the comparison with the ALFALFA/JCMT sample is difficult because of a lack of objects. There a comparison with the LV sample is more appropriate. In this mass range the VGS galaxies tend to be more gas rich then their LV counterparts, giving the general impression that in particular towards lower stellar masses the VGS galaxies are gas rich systems.

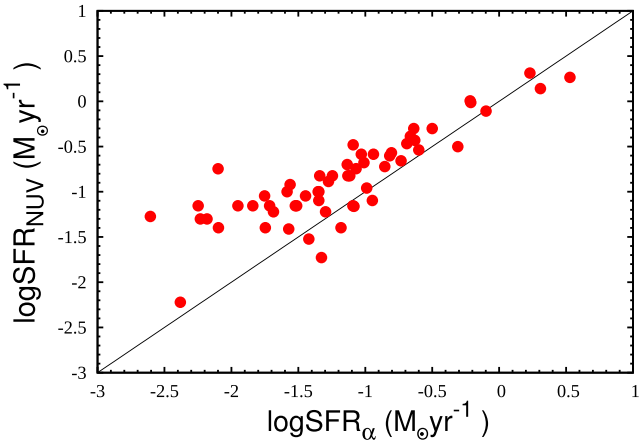

Figure 6. SFR α against SFR_{NUV} of the VGS galaxies.

5.2 Current and recent star formation properties

There are many studies in the literature comparing the two star formation tracers H α and NUV. Such a study, however, has never been specifically carried out for void galaxies. Here, we interpret our results using previous studies which have investigated both these two regimes. First, we compare the two star formation tracers in Fig. 6, then we examine the H α and NUV star formation rates of the VGS galaxies as a function of $g - r$ colour and stellar mass. For each relation, we present these scaling relations derived from the H α and the NUV fluxes after a correction for extinction.[7] In general, we see similar trends to those observed in previous studies. According to Fig. 6, SFR α is systematically lower than SFR_{NUV} at star formation rates below SFR $\alpha \sim 0.03\ M_\odot\ yr^{-1}$. This discrepancy between H α and UV star formation rates has been investigated in several studies (Sullivan et al. 2000; Bell & Kennicutt 2001; Buat et al. 2002; Lee et al. 2009b, 2011; Karachentsev & Kaisina 2013). In most cases, they compared H α to far-UV, instead of to NUV. The main result is that, after applying proper corrections for dust attenuation, H α tends to increasingly underpredict the total SFR relative to the far-UV at the faint end of luminosity function ($L\,\alpha \leq 10^{37}$ erg s^{-1}). Lee et al. (2009b) showed that the average H α to far-UV flux ratio is lower than expected by a factor of 2, at SFR $\alpha \sim 0.003\ M_\odot\ yr^{-1}$. In our sample this decrease is much more prominent and steep and starts at around SFR $\alpha = 0.03\ M_\odot\ yr^{-1}$. Several suggestions have been made to explain the observed trends in SFR α/SFR_{FUV}. These include: the effects of uncertainties in the stellar evolution tracks and model atmospheres, non-solar metallicities, non-constant star formation histories (SFHs), leakage of ionizing photons, departures from Case B recombination, dust attenuation, stochasticity in the formation of high-mass stars and variations in the initial mass function (see Lee et al. 2009b; Meurer et al. 2009, for a review). The VGS galaxy sample contains many low-mass galaxies. In particular the VGS galaxies with very low star formation rates have stellar masses around $10^8\ M_\odot$ and lower, and as we will discuss in Section 5.4, the VGS galaxy sample consists

[7] As it will be discussed in the following sections, our sample consists of an AGN. However, it is not plotted, since we cannot distinguish the AGN from the H α emitting disc.

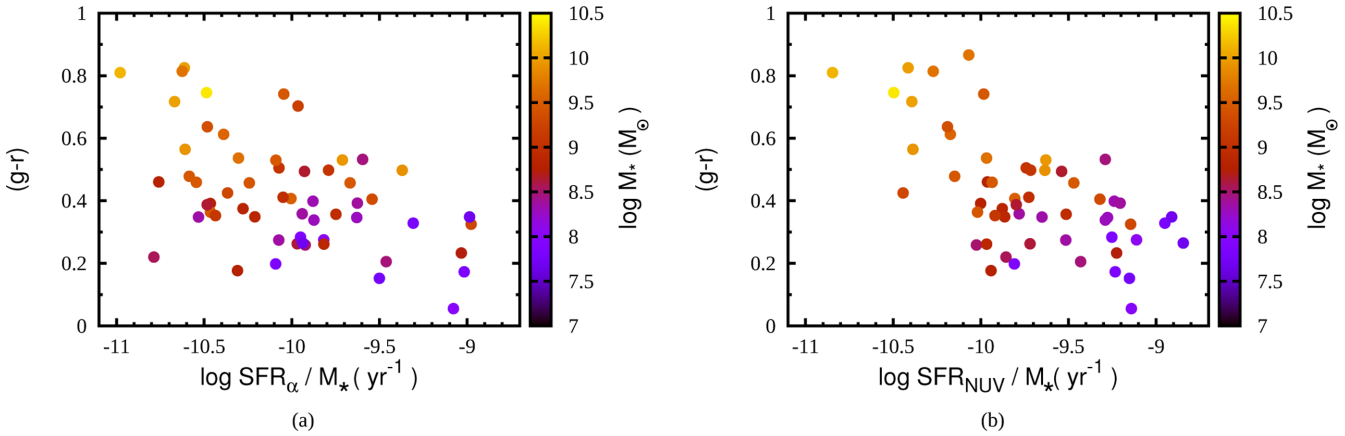

Figure 7. Left: $(g - r)$ colour versus Hα S_SFRs (SFRα/M_*) of the VGS galaxies, colour coded as a function of their stellar mass. Right: similar to the previous plot except that $(g - r)$ is plotted against the NUV S_SFRs (SFR$_{UV}/M_*$). There is a tighter correlation compared to the Hα case.

of galaxies with quite a range in metallicity. So it is important to bear this difference between UV and Hα SFRs in mind.

In Fig. 7, we compare $(g - r)$ colour of the VGS galaxies with their specific star formation rates (SFR/M_*), computed for both Hα (Fig. 7a) and NUV (Fig. 7b). We add the stellar masses as a third parameter in this comparison and plot the VGS galaxies, colour coded as a function of their stellar mass. According to the colour-star formation-stellar mass relation, smaller galaxies are in general bluer and have higher S_SFRs for a given mass range (Brinchmann et al. 2004; Kauffmann et al. 2004). VGS galaxies display the expected trend although there is a difference between the Hα and NUV regimes. It is clear that this difference depends on stellar mass. For the Hα, there is no single linear correlation for the whole stellar mass range (Fig. 7a). Both low- and high-mass galaxies are present for a given SFRα/M_* range. In the NUV domain, however, there is a tighter linear relation between colour and NUV S_SFRs (Fig. 7b). Besides, galaxies are uniformly distributed in this linear relation with respect to their stellar mass; low stellar mass galaxies have higher S_SFRs and are blue, higher stellar mass ones have lower S_SFRs and are red. This supports the hypothesis that small galaxies suffer much more from stochasticity, affecting Hα samples more as Hα is more sensitive to the very recent star formation (time-scale is 5×10^6 yr for Hα and 10^7 yr for UV), as noted by Lee et al. (2009b).

The majority of the VGS galaxies have SFRα less than 1 M$_\odot$ yr^{-1}. The mean SFRα is $\sim 0.1 \pm 0.03$ M$_\odot$ yr^{-1} and the luminosities range between $\sim 3 \times 10^{38}$ erg s^{-1} $<$ L$\alpha \lesssim 2.4 \times 10^{41}$ erg s^{-1}. When corrected for the extinction, the mean SFRα becomes $\sim 0.2 \pm 0.06$ M$_\odot$ yr^{-1} and the luminosity increases to 6×10^{41} erg s^{-1}.

Similar to the Hα star formation rates, most of the galaxies have SFR$_{NUV}$ below 1 M$_\odot$ yr^{-1}. The mean SFR$_{NUV}$ of the VGS galaxies is ~ 0.08 M$_\odot$ yr^{-1}, and ~ 0.35 M$_\odot$ yr^{-1} when corrected for internal extinction.

In Fig. 8, we compare the SFRα of the VGS and the comparison sample galaxies to their gas fractions $M_{H\,I}/M_*$. The SFRα of the VGS galaxies increases as their gas fractions decrease. This is true for the ALFALFA and the JCMT galaxies as well. LV galaxies, on the other hand, populate the area with gas fractions below 1 and SFRα < 0.1 M$_\odot$ yr^{-1}, and do not show a significant trend in SFRα with decreasing gas fraction.

When comparing the SFRα to M_B (Figs 9 a and b), both the VGS galaxies and the comparison sample display the well-known

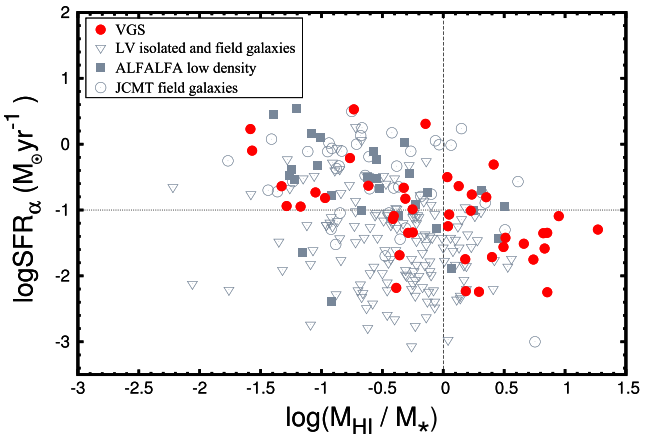

Figure 8. The extinction corrected SFRα plotted against the $M_{H\,I}$-to-M_* ratios for the VGS galaxies and the comparison sample.

star formation – luminosity correlation, with VGS galaxies having a slope of -0.5. This is steeper than the slope of -0.29 and -0.41 found by Sánchez-Gallego et al. (2012) and Lee et al. (2009a), respectively. The ALFALFA sample has a very similar slope as the VGS galaxies, while the JCMT sample shows large scatter and a shallower slope.

Many LV galaxies have much lower luminosities than the VGS galaxies and they have a large spread in their SFRs at the low luminosity end (Fig. 9b). The same is true for the VGS galaxies although they do not probe as low luminosities as the LV galaxies do. There is only one VGS galaxy with M_B fainter than -15.

Despite the large range in luminosity covered by the VGS galaxies and the comparison samples and the scatter in the data, it is quite remarkable that all obey the star formation – luminosity correlation so well.

5.3 Colour and star formation properties

The IR data can be used to probe the old stellar population as well as the more recent star formation. The *WISE* 3.4 and 4.5 μm bands are dominated by old stellar populations and sensitive to hot dust whereas the 12 μm band is sensitive to star formation and dust continuum, and dominated by 11.3 μm polycyclic aromatic hydrocarbon (PAH) emission. The colour–colour diagram of these

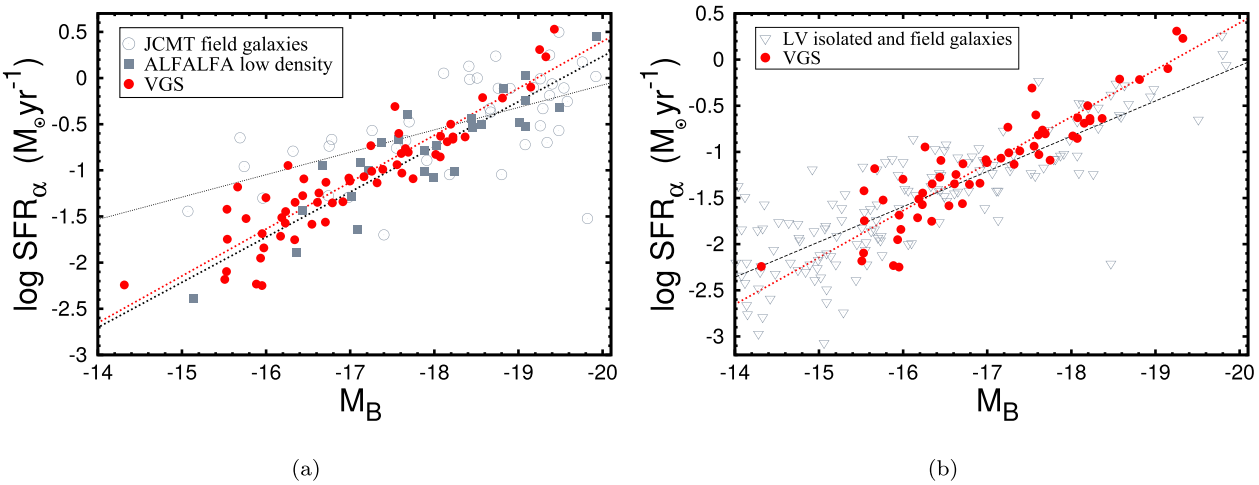

Figure 9. (a) and (b): the extinction corrected SFR α against M_B for the VGS galaxies and the comparison sample. Best fits for the VGS galaxies (logSFR $\alpha = -0.5 \times M_B - 9.77$), JCMT field galaxies (logSFR $\alpha = -0.25 \times M_B - 5$), ALFALFA Virgo surrounding (logSFR $\alpha = -0.49 \times M_B - 9.56$) and LV samples (logSFR $\alpha = -0.4 \times M_B - 7.95$) are indicated with the dashed lines.

bands has been shown to be an efficient way of separating old stellar population dominated systems from star-forming systems and active galactic nuclei (AGNs; Jarrett et al. 2011; Stern et al. 2012; Cluver et al. 2014). In Fig. 10(a), we overplot VGS galaxies that have high S/N detections at 3.4 and 4.5 μm on the *WISE* colour–colour diagram of Jarrett et al. (2011). VGS galaxies lie on the green zone of spiral galaxies. Their colour [4.6]–[12] > 1.5 is consistent with actively star-forming systems. Some of the peculiar examples of our sample are also indicated on the plot. VGS_31 and 31a are two Markarian galaxies and have the highest SFRs of the whole sample. They occupy a region overlapping with starbursts. The AGN VGS_24 is clearly separate from the rest of the VGS galaxies and closer to the region of QSOs, Seyferts and AGNs. VGS_05 is very blue (in [3.4]–[4.6] colour) in the infrared as most early-type galaxies. Galaxies in the *WISE* colour–colour diagram are plotted together with the rest of the VGS galaxies in an optical colour–magnitude diagram in Fig. 10(b). In this diagram, we show the relation between the SDSS $g - r$ colour, the absolute B-band magnitude and the Balmer decrement of the VGS galaxies. Galaxies plotted in Fig. 10(a) are indicated as dots and the remaining galaxies as squares. Most of the red galaxies in Fig. 10(b) have higher Balmer decrement values ($4 \leq \mathrm{H}\alpha/\mathrm{H}\beta \leq 6$) and are also detected at 3.4, 4.6 and 12 μm. This shows that these objects are red (in $g - r$ colour) due to extinction and they are not early-types galaxies that still form stars.

The distribution of the VGS galaxies in the *WISE* colour–colour diagram and in the optical colour–magnitude diagram suggest that these objects have a significant old stellar population as well as young population which is also found by Penny et al. (2015). On the other hand, blue and small galaxies in Fig. 10(b) (except a couple of objects), have smaller Balmer decrement values so they are not significantly affected by extinction. The fact that they are blue and not bright in *WISE* bands show that these galaxies are dominated mostly by young stars. For fainter galaxies the metallicity is lower, so the extinction as well, therefore it is difficult to say anything about the amount of old stars.

5.4 Metallicity and mid-infrared star formation rate

The *Spitzer* 24 μm band is sensitive to warm-dust emission and a good tracer of star formation (Calzetti et al. 2007; Rieke et al. 2009). As shown in Jarrett et al. (2013) there is a tight correlation between *WISE* 22 μm and *Spitzer* 24 μm luminosities since they are close in wavelength.[8] The *WISE* 12μm band, on the other hand, is more sensitive than the *WISE* 22 μm band and probes the interstellar medium. It is also a good indicator of star formation as it is dominated by 11.3 μm PAH feature that is excited by ultraviolet radiation from young stars, as well as radiation from older stars (Jarrett et al. 2013; Cluver et al. 2014 and references therein). Lee, Hwang & Ko (2013) also showed that both 12 and 22 μm luminosities correlate well with H α SFR estimates, concluding that both bands are good SFR indicators of dusty galaxies, but suffer from a metallicity bias. It is therefore important to examine metallicity as well. In this section, we study the relation between the H α and the mid-infrared star formation rates, and the metallicity of the VGS galaxies. In Fig. 11, we examine the relation between the star formation rates derived from the *WISE* 12 and 22 μm luminosities and H α following the studies mentioned above. First, we compare the 22 μm SFR (SFR_{22}) to SFR α (Fig. 11a) and then the 12 μm SFR (SFR_{12}) to SFR α (Fig. 11b). In both diagrams, we use the gas-phase metallicity, 12+log(O/H), taken from the MPA/JHU catalogue for SDSS DR7 (see Section2.4.1), as a third parameter. Galaxies that are not present in this catalogue due to low S/N on the emission lines are shown as black squares. Both SFR_{22} and SFR_{12} correlate well with SFR α as found by Lee et al. (2013) and Cluver et al. (2014). At low star formation rates, around logSFR $\alpha \leq -0.5$ $\mathrm{M}_\odot\ \mathrm{yr}^{-1}$, SFR_{12} tends to underestimate the SFRs. This is also observed by Lee et al. (2013) and Cluver et al. (2014). A possible explanation for this is the effect that low-metallicity could change the relative abundance of PAH molecules to big grains, and thereby affecting the total emission (Lee et al. 2013; Cluver et al. 2014). Indeed the VGS galaxies in the low SFR_{12} range have lower metallicities. On the other hand this discrepancy is not observed between SFR_{22} and SFR α by either of these authors.

The mass-metallicity-star formation relation of the VGS galaxies shown in Fig. 12 supports the observed trend in Fig. 11. Here, we plot the mass–metallicity relation as a function of both SFR α (Fig. 12a) and SFR_{12} (Fig. 12b). In both diagrams

[8] The *WISE* 22 μm band is closer to 23 μm (hence, very similar to *Spitzer* MIPS 24 μm), as determined by Brown et al. (2014).

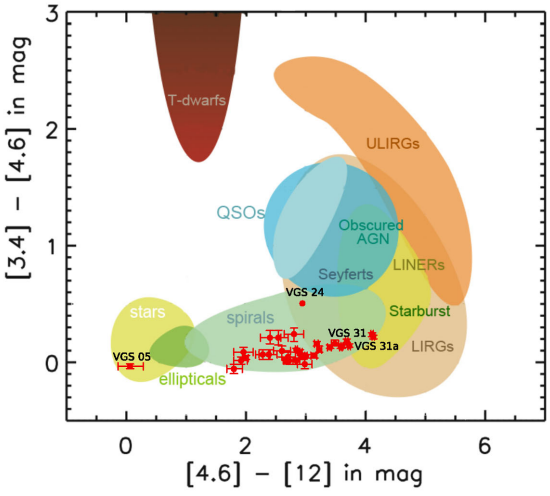

(a)

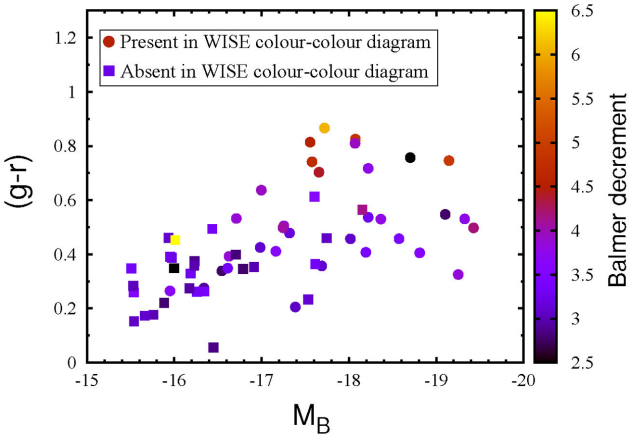

(b)

Figure 10. (a) VGS galaxies (red dots) overlaid on the *WISE* [3.4]–[4.6] against [4.6]–[12] colour–colour diagram (without *k*-corrections) adapted from Jarrett et al. (2011). Only the objects with magnitude error < 0.2 mag in both colours are shown. Some of the particular examples in the VGS sample are indicated. VGS_05; an early-type galaxy, VGS_24; which is the only AGN and Markarian galaxies VGS_31 and 31a are labeled in the diagram as well. (b) Colour–magnitude diagram based on SDSS $g - r$ colour. Galaxies that are plotted in (a) shown as dots and galaxies that are absent in the colour–colour diagram are shown as squares.

VGS galaxies follow the mass–metallicity relation of Tremonti et al. (2004); metallicity decreases with decreasing mass. Galaxies with low star formation rates have lower metallicity. This trend is clearer in the 12 μm than in the Hα regime where galaxies with similar SFRα have different mass. On the other hand at 12 μm galaxies are uniformly distributed in this linear relation with respect to their stellar mass. In conclusion, the relation between the mid-infrared and optical star formation rate tracers suggests that the VGS sample consists of both dusty high metallicity galaxies and less dusty low metallicity galaxies with in general lower star formation rates. As for the emission line properties, VGS galaxies follow the same characteristics as other star-forming galaxies, even including having an occasional AGN (1 out of 59) and exhibiting similar proportions of normal star-forming galaxies and starbursts, i.e. based on emission line ratios when put in a BPT diagram (Fig. 13a). Fig. 13(b) shows the VGS galaxies colour coded as a function of their total H I mass. It is clear that the inferred excitation does not depend on H I mass.

11 galaxies in the low metallicity – high excitation zone have similar properties to the starburst dwarf galaxies. They are not detected in 22 μ, suggesting they do not have much dust. In their spectra, they exhibit very strong Hα and [O III] emission lines.[9] Given these facts, they seem to be metal poor, and their position in the BPT diagram ($\log(\mathrm{N\,II}/\mathrm{H}\alpha) < -0.9$) confirms this (Fig. 13a).

5.5 Dependence of star formation on H I surface density

The Kennicutt–Schmidt (KS) law (Kennicutt 1998) describes the relation between the surface density of star formation and the surface density of gas (H I + H_2). The KS law was originally applied to global properties, but has also been demonstrated (Bigiel et al. 2008; Kennicutt & Evans 2012) to describe the local relation between SF surface density and gas density within galaxies. Since we do not know the H_2 content of our galaxies (except VGS_31a; Beygu et al. 2013) and our H I data is not good enough for a spatial KS law analysis we examined the global KS law for the VGS galaxies. To do this we have selected 18 VGS galaxies within our sample for which we can resolve the H I surface density distribution within the galaxy disc.[10] We calculated the average surface densities of star formation and H I within the Petrosian R90 radius taken from SDSS DR7 (the radius containing 90 per cent of Petrosian flux; Petrosian 1976). The Petrosian R90 radius can be considered a representative radius for calculating average surface densities since the Hα emission of the VGS galaxies does not extend beyond this radius. In Fig. 14, we show the global KS law for the 18 resolved VGS galaxies determined from the Hα and also compare them with the sample of spiral galaxies from Kennicutt (1998).

Fig. 14 covers the range of Σ_{SFR} and $\Sigma_{\mathrm{H\,I}}$ where normal and low surface brightness galaxies are mostly located. We do not see a strong correlation between the Σ_{SFR} and the $\Sigma_{\mathrm{H\,I}}$ of the VGS galaxies but rather a large spread. A similar behaviour is shown by the low surface brightness galaxies in Kennicutt (1998). For the spiral galaxy sample studied in Kennicutt (1998), even after including the H_2 to the gas density, a large scatter is still present (Fig. 2 in that paper). In the same paper an attempt was made to examine the SFR versus the H I density relation for a larger sample of spiral galaxies (Fig. 4 in that paper), however the large dispersion is still present. The correlation is very similar to Fig. 14 as well and as Kennicutt (1998) stated the physical interpretation of the SFR versus H I Schmidt law is not obvious, and complicated by the mutual effects of the UV field associated with the recent star formation and the balance between the atomic and molecular fraction of the neutral hydrogen in this low-density regime.

In Fig. 15, we show the relation between the Hα star formation rate and the total H I mass for the VGS galaxies and the comparison sample. We also plot additional data from The *Spitzer* Infrared Nearby Galaxies Survey (SINGS) galaxy sample (Cluver et al. 2010) that consists of infrared imaging and spectroscopic survey of 75 nearby galaxies. In Fig. 15 three linear fits are shown; the VGS galaxies (red solid line), the comparison sample together (grey solid line) and the SINGS galaxies (black dotted line). We excluded

[9] Their apparent sizes are ∼ of 3 arcsec SDSS fibre aperture, so the SDSS spectra can be considered as representative of the whole galaxy disc.
[10] Kreckel et al. (2012) found that most of the VGS galaxies have H I discs two to three times more extended than their stellar discs.

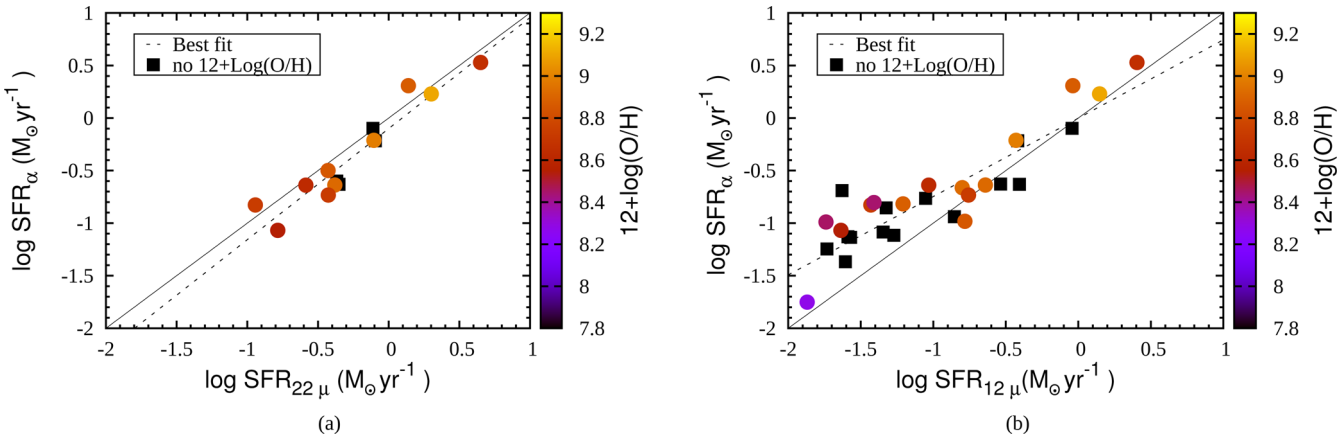

Figure 11. (a): SFR$_{22}$ against SFR α as a function of gas-phase metallicity. (b): same as the previous plot, except that SFR$_{12}$ is plotted instead of SFR$_{22}$. In both diagrams black lines correspond to a one-to-one correlation while the dashed lines are the best fit. Black squares are the galaxies that are not present in the gas-phase metallicity catalogue of the MPA/JHU catalogue for SDSS DR7.

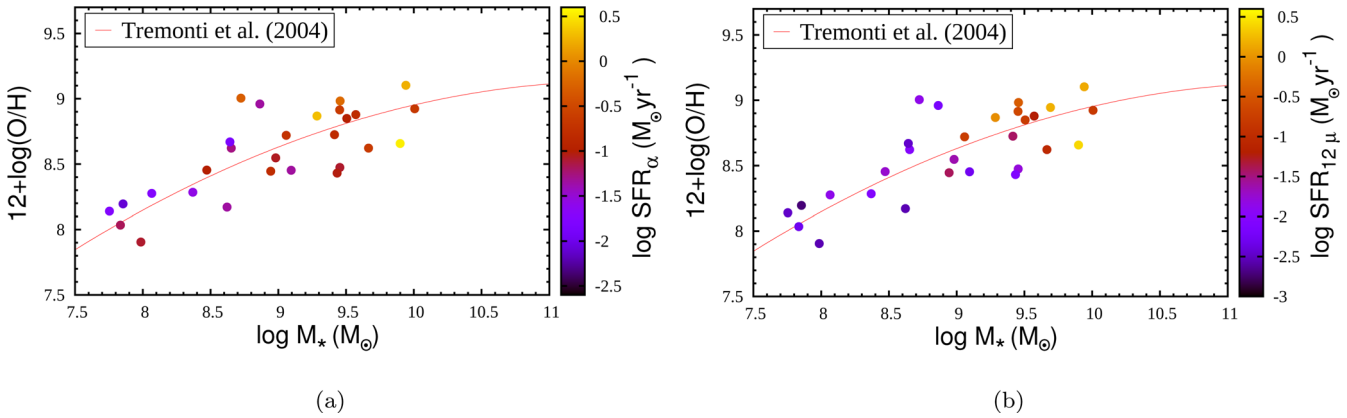

Figure 12. Mass–metallicity relation for the VGS galaxies as a function of SFR α (a) and SFR$_{12}$ (b). Mass–metallicity relation of Tremonti et al. (2004) is indicated as a red line.

eight VGS galaxies (shown as black dots) with logSFR $\alpha/M_{\rm H\,I} > 10^{-9}$ yr^{-1} from the fit. These are the objects that have significantly elevated SFR for a given H I mass, also clearly seen in the top panel of Fig. 16(a). Overall each comparison sample display a linear relation similar to SINGS galaxies (Cluver et al. 2010). VGS galaxies, however, scatter above the relation indicating more elevated SFR for a given total H I mass. This indicates that the VGS galaxies have higher star formation rate for their total H I content. We will discuss this further in the next section.

5.6 Specific star formation and star formation efficiencies.

For a proper comparison of star formation properties it is important to normalize the observed star formation rates. This can be done in different ways. It has become customary to normalize to the stellar mass (giving a S_SFR) or to the gas mass (giving a star formation efficiency). Here, we use both measures for both the VGS galaxies and the galaxies in the comparison samples, making sure that the star formation rates and stellar masses have been determined using the same methods.

In Figs 16 and 17, we compare the S_SFR (SFR α/M_*) and star formation efficiency (SFR $\alpha/M_{\rm H\,I}$) of the VGS galaxies to those of field galaxies from the comparison samples.

It is clear from Figs 16 and 17 that SFR α/M_* and SFR $\alpha/M_{\rm H\,I}$ of the VGS galaxies as a function of M_* and $M_{\rm H\,I}$ behave in a similar way as those of the field galaxies in our comparison samples. In Figs 16(b) and 17(b), we plot the mean of the SFR α/M_* and SFR $\alpha/M_{\rm H\,I}$ per 0.5 dex of $M_{\rm H\,I}$ and M_*. Although not each mass bin is uniformly filled both by the VGS and the comparison sample galaxies, it is still possible to derive statistical information. Below we discuss SFR $\alpha/M_{\rm H\,I}$ and SFR α/M_*.

In Fig. 16, the VGS and the comparison sample galaxies have similar SFR $\alpha/M_{\rm H\,I}$ and SFR α/M_* as a function of $M_{\rm H\,I}$, except at $M_{\rm H\,I} < 10^9$ M$_\odot$ and $M_{\rm H\,I} \geq 10^9$ M$_\odot$. At $M_{\rm H\,I} < 10^9$ M$_\odot$, VGS galaxies have slightly higher SFR $\alpha/M_{\rm H\,I}$ than the comparison sample of LV galaxies which is the only sample of comparison galaxies populating this mass range. This is expected as shown in Fig. 15. At $M_{\rm H\,I} > 10^9$ M$_\odot$, VGS galaxies do not have notably different SFR $\alpha/M_{\rm H\,I}$ than the comparison sample. This mass range is mostly populated by the JCMT galaxies and subsequently by the ALFALFA galaxies. The SFR α/M_* of the VGS galaxies appears to be slightly higher than that of the comparison samples over the entire stellar mass range, though the difference is very small.

When corrected for extinction both the SFR $\alpha/M_{\rm H\,I}$ and SFR α/M_* of the VGS galaxies and the comparison sample galaxies as a function of M_* (Fig. 17) are very similar, except that two VGS galaxies around $M_* = 10^{10}$ M$_\odot$ stand out with higher SFR $\alpha/M_{\rm H\,I}$ (Fig. 17a, top panel). These are VGS_31a and VGS_57.

Overall, the star formation efficiency is very constant over the range of stellar masses covered while the S_SFR decreases with

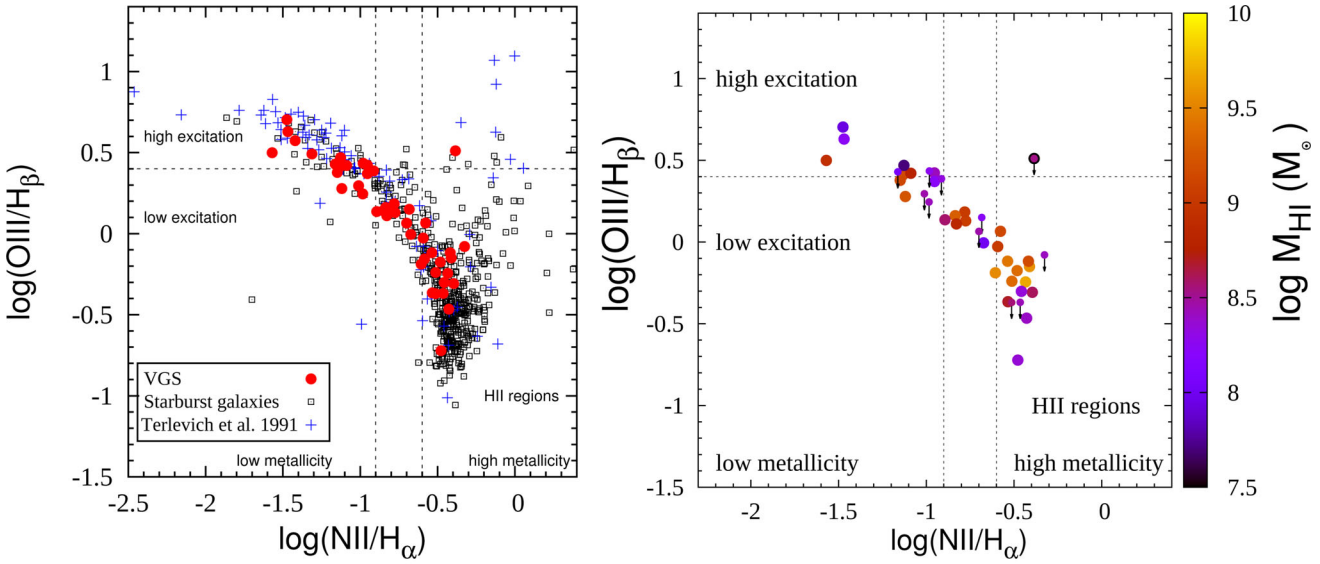

Figure 13. Left: the BPT diagram showing the ratio of emission line fluxes of [O III]/H β to [N II]/H α of the VGS galaxies. Red filled circles are VGS galaxies selected as explained in Section 3.3.1. The comparison sample of emission-line galaxies has been constructed from the emission-line galaxy sample of Terlevich et al. (1991). Galaxies defined as starbursts are taken from the SIMBAD and from Coziol (2003) where in the latter, they are defined as starburst Markarian galaxies. This diagram is adapted from Raimann et al. (2000). The point at the top right of the panel is the only AGN, VGS_24, in our VGS galaxy sample. Right: same as left-hand panel, except that only VGS galaxies are shown as a function of the logarithm of their H I masses. Galaxies with upper H I detection limit are shown with arrows.

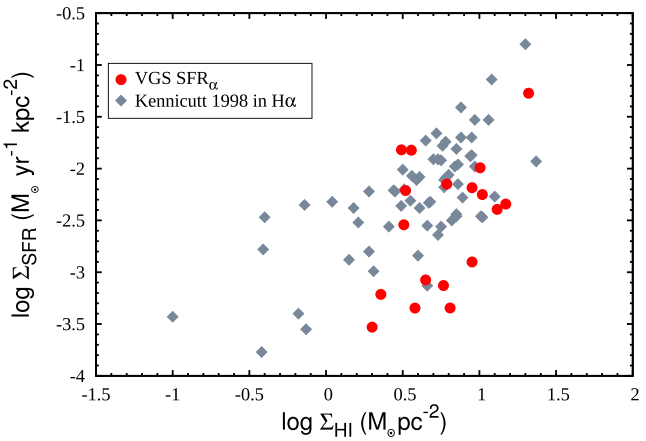

Figure 14. Correlation of the disc-averaged H α (red dots) SFRs with the surface densities of H I. Grey diamonds indicate the spiral galaxies from Kennicutt (1998).

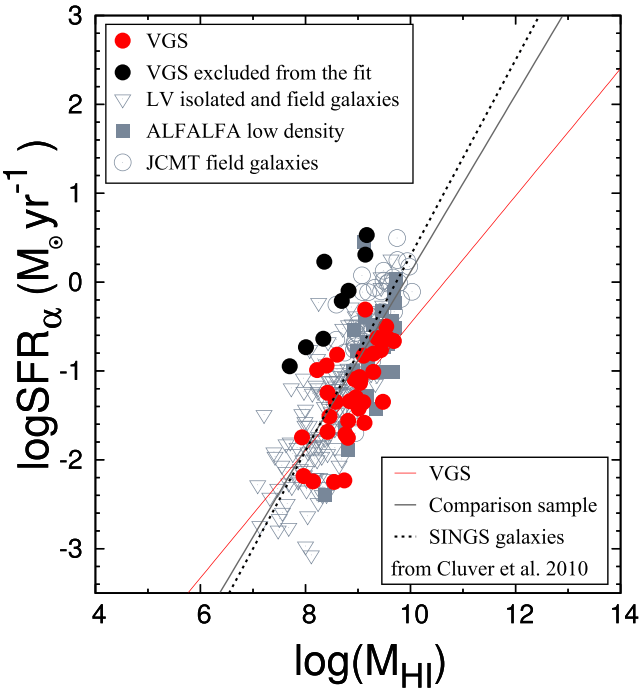

Figure 15. SFR α against the total H I mass of the VGS galaxies, the comparison sample and the SINGS galaxies from Cluver et al. (2010). Linear least-squares fits are made through the VGS galaxies (red solid line), the comparison sample (grey solid line) and the SINGS galaxies (black dotted line). VGS galaxies that have significantly elevated SFR for a given H I mass (black dots) are excluded from the fit.

increasing stellar mass, as already noted by Kreckel et al. (2012) using SFRs extrapolated from the H α fluxes from the SDSS DR7 fibre spectra. The decrease in SFR α/M_* is about a factor 10 over a hundredfold increase in stellar mass from 10^8 to 10^{10} $M_\odot$. This trend is not specific to galaxies in voids but also present in galaxies in slightly denser environments.

6 DISCUSSION

Voids and void galaxies are very suitable candidates to test and study two of the most important theories on galaxy formation and evolution. These are related to the formation of dwarf galaxies and the role of cold gas accretion.

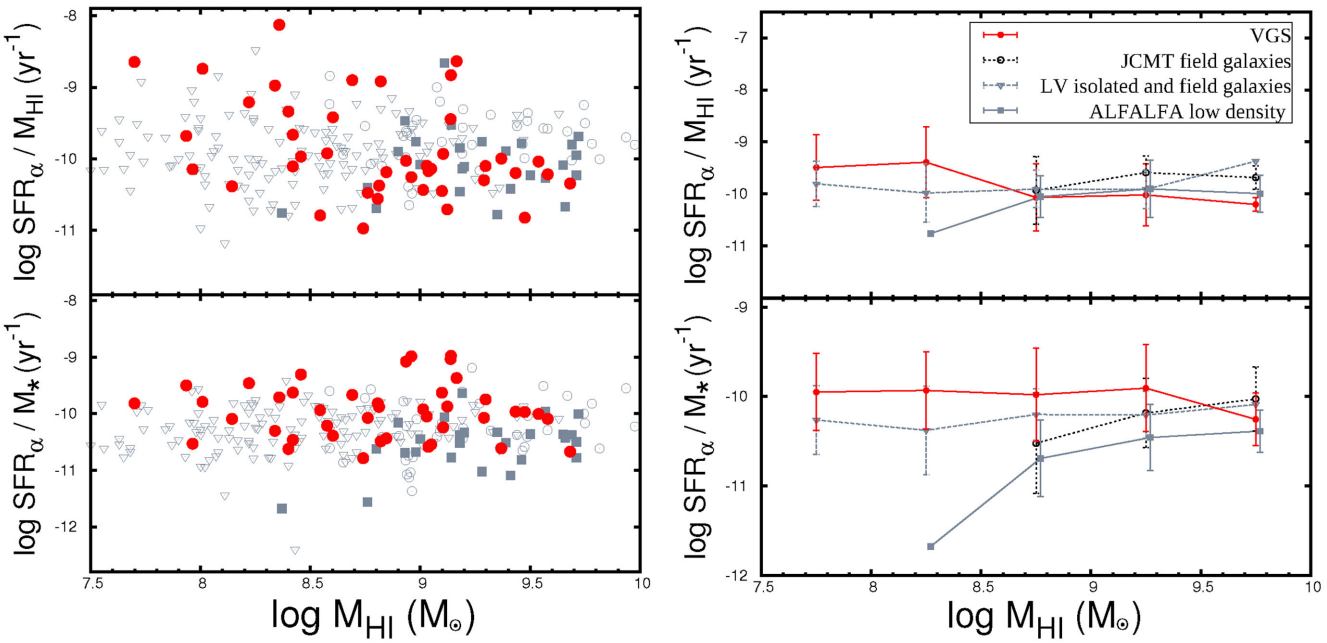

Figure 16. Left-hand panel: the extinction corrected SFR α normalized by the $M_{\rm H\,I}$ (top) and normalized by the M_* (bottom) are plotted against the $M_{\rm H\,I}$ for the VGS galaxies and the comparison sample. Right-hand panel: the mean of the SFR $\alpha/M_{\rm H\,I}$ and SFR α/M_* are plotted per 0.5 dex of $M_{\rm H\,I}$ (only for detections) for the distributions shown on the left-hand panel.

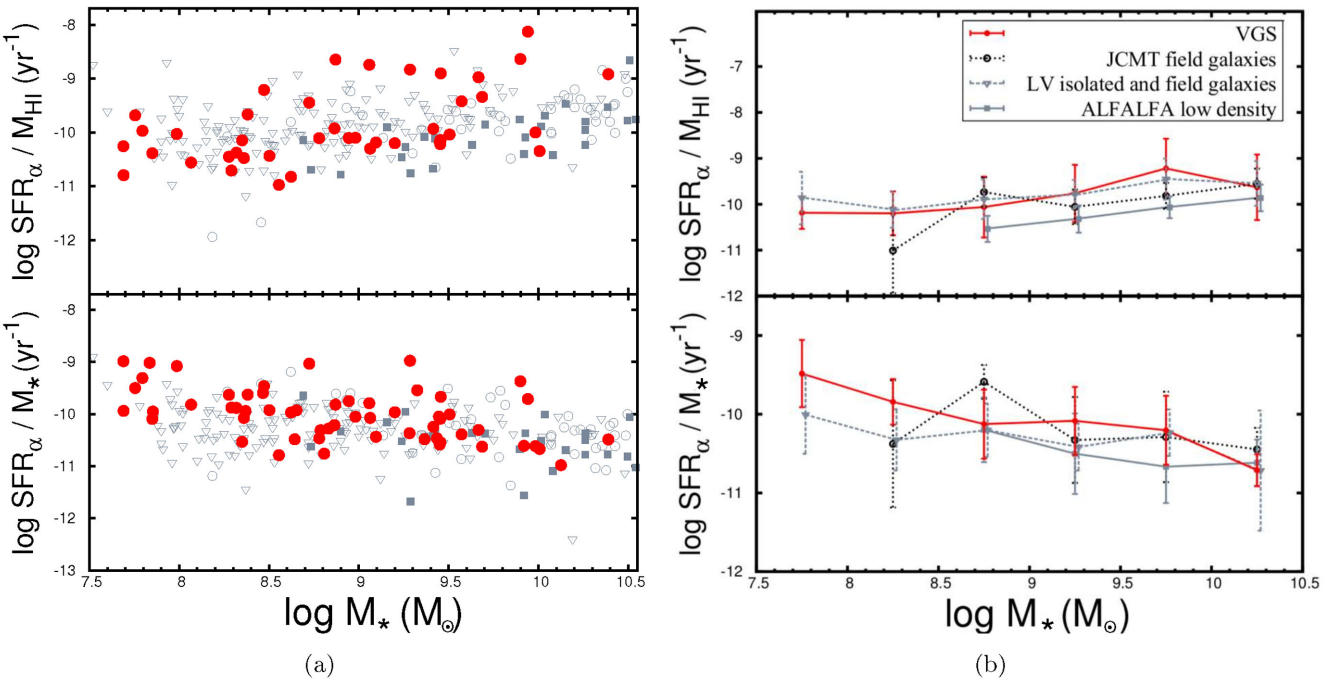

Figure 17. Left-hand panel: the extinction corrected SFR α normalized by the $M_{\rm H\,I}$ (top) and normalized by the M_* (bottom) are plotted against the M_* for the VGS galaxies and the comparison sample. Right-hand panel: the mean of the SFR $\alpha/M_{\rm H\,I}$ and SFR α/M_* are plotted per 0.5 dex of M_* (in the SFR $\alpha/M_{\rm H\,I}$ case, only for the H I detections) for the distributions shown on the left-hand panel.

Although void galaxies in our sample are mostly blue and small galaxies with stellar masses below 3×10^{10} $M_{\odot}$, we do not detect the missing dwarf galaxy population (Kreckel et al. 2012) whose absence was stressed by Peebles (2001) as a major riddle for our understanding of galaxy formation. A simple observational ground for this could be the difficulty in detecting these objects at this redshift range ($0.02 < z < 0.03$). The reason why these galaxies are not included in our VGS sample is that they remain undetected as the VGS galaxies have been selected within the SDSS spectroscopic flux limit of 17.7 mag in *r* band. On the other hand, if their absence in the VGS sample is the reflection of a true physical phenomenon, it may be the result of some interesting astrophysical process. One of the most suggestive one is the proposition of Hoeft & Gottlöber (2010). They argue that photoheating due to the cosmic UV background stops gas condensation in the haloes of these small galaxies. In their simulations, Hoeft & Gottlöber (2010) show that the already condensed gas can be retained by these haloes. This gas would be allowed further star formation. However, as mentioned above, our observations may simply not be sensitive enough to detect these dwarf galaxies affected by photoheating.

Another interesting physical process was first discussed by Dekel & Birnboim (2006). They proposed that the galaxy bimodality (blue and red sequence) in the colour–magnitude space could be understood by looking at the thermal properties of the inflowing gas, in particular the role and presence of cold accretion flows. According to their model, the blue sequence galaxies below a characteristic stellar mass $M_{*,\mathrm{crit}} \simeq 3 \times 10^{10}$ $M_{\odot}$, reside in haloes whose mass is below a critical shock-heating mass. In these haloes, the disc is built by cold flows and might generate early starbursts (Dekel & Birnboim 2006).

Simulations by Kereš et al. (2005) also suggested that low-density regions today are dominated by cold mode accretion. Since void galaxies in our sample are all below $M_{*,\mathrm{crit}}$, this would suggest that cold accretion dominates. It would imply that they too form an ideal sample to study cold flow dominated galaxy evolution further. Moreover, the tenuous large-scale structure around void galaxies determines the way a galaxy may accrete mass in terms of direction and more importantly, the coherence of the infalling matter (Aragón-Calvo & Szalay 2013; Rieder et al. 2013).

Our study indicates that galaxies in voids are similar in their star formation properties to galaxies in slightly denser environments in the nearby universe. The only notable difference is that the S_SFR maybe slightly enhanced by 0.2 dex. This may indicate a slightly more steady (and less disrupted) inflow of gas in the picture of cold accretion. To put the star formation properties of void galaxies in the context of their formation history, we plan to study in more detail their molecular hydrogen content as well as their metallicity and their star formation histories. This will allow us to put further constraints on the place of these void galaxies in the general context of galaxy formation. In an accompanying paper, we will discuss the morphology and colour properties of these void galaxies (Beygu et al., to be submitted)

7 CONCLUSIONS

We have examined the star formation properties of the VGS galaxies and compared them with field galaxies. The main conclusions are

(i) The S_SFR of the VGS galaxies follows the same decreasing trend with stellar mass as galaxies in somewhat denser environments (Figs 16 and 17). The star formation efficiencies are fairly constant with stellar mass, although their SFR is slightly elevated at $M_{\mathrm{H\,I}} < 10^9$ $M_{\odot}$ for their total H I content. These are more difficult to interpret as explained in Section 3.6.4. The S_SFR with stellar mass $M_{\odot}$, is slightly elevated in the void galaxies.

(ii) VGS galaxies display a wide range in dust content and metallicity. The sample consists of dusty and high metallicity galaxies as well as galaxies with insignificant dust content and low metallicity.

(iii) The VGS galaxies appear to obey the canonical 'star formation main sequence' uncovered in galaxies in general (Kennicutt 1998; Tremonti et al. 2004), indicating that the star formation process progresses under similar physical conditions as in galaxies in environments somewhat denser than voids.

(iv) There is no strong correlation between the Hα formation properties of the VGS galaxies and their H I content.

ACKNOWLEDGEMENTS

The authors wish to thank Michael Vogeley, for a careful assessment of the manuscript and very useful comments. BB is grateful to Jarle Brinchmann and Daniela Calzetti for many helpful discussions and insightful thoughts and also wishes to thank I.D. Karachentsev and J. R. Sánchez-Gallego for their help in use of their catalogues, and to thank Marius Cautun, Peppo Gavazzi and Manolis Papastergis. We would like to thank M. Querejeta and S. Meidt for sharing their S4G nearby galaxy stellar mass catalogue. This work was supported in part by the National Science Foundation under grant no. 1009476 to Columbia University. We are grateful for support from a Da Vinci Professorship at the Kapteyn Astronomical Institute. JMH acknowledges support from the European Research Council under the European Union's Seventh Framework Programme (FP/2007-2013)/ ERC Grant Agreement no. 291531. KK acknowledges grants 4598/1-2 and SCHI 536/8-2 from the DFG Priority Program 1573. MDM observatory is located on the southwest ridge of Kitt Peak, home of the Kitt Peak National Observatory, Tucson, Arizona. The Observatory is owned and operated by a consortium of five universities: the University of Michigan, Dartmouth College, the Ohio State University, Columbia University and Ohio University. We acknowledge KPNO for the use of their Hα filters. The INT is operated on the island of La Palma by the Isaac Newton Group in the Spanish Observatorio del Roque de los Muchachos of the Instituto de Astrofísica de Canarias.

REFERENCES

Aragón-Calvo M. A., Szalay A. S., 2013, MNRAS, 428, 3409
Aragón-Calvo M. A., van de Weygaert R., Jones B. J. T., 2010, MNRAS, 408, 2163
Balogh M. L., Morris S. L., Yee H. K. C., Carlberg R. G., Ellingson E., 1999, ApJ, 527, 54
Bell E. F., Kennicutt R. C., Jr, 2001, ApJ, 548, 681
Beygu B., Kreckel K., van de Weygaert R., van der Hulst J. M., van Gorkom J. H., 2013, AJ, 145, 120
Bigiel F., Leroy A., Walter F., Brinks E., de Blok W. J. G., Madore B., Thornley M. D., 2008, AJ, 136, 2846
Blanton M. R., Roweis S., 2007, AJ, 133, 734
Brinchmann J., Charlot S., White S. D. M., Tremonti C., Kauffmann G., Heckman T., Brinkmann J., 2004, MNRAS, 351, 1151
Brown M. J. I., Jarrett T. H., Cluver M. E., 2014, PASA, 31, 49
Buat V., Boselli A., Gavazzi G., Bonfanti C., 2002, A&A, 383, 801
Calzetti D., 2001, PASP, 113, 1449
Calzetti D., Armus L., Bohlin R. C., Kinney A. L., Koornneef J., Storchi-Bergmann T., 2000, ApJ, 533, 682
Calzetti D. et al., 2007, ApJ, 666, 870
Cappellari M., Emsellem E., 2004, PASP, 116, 138
Cardelli J. A., Clayton G. C., Mathis J. S., 1989, ApJ, 345, 245

Cautun M., van de Weygaert R., Jones B. J. T., Frenk C. S., 2014, MNRAS, 441, 2923
Ceccarelli L., Padilla N. D., Valotto C., Lambas D. G., 2006, MNRAS, 373, 1440
Cluver M. E., Jarrett T. H., Kraan-Korteweg R. C., Koribalski B. S., Appleton P. N., Melbourne J., Emonts B., Woudt P. A., 2010, ApJ, 725, 1550
Cluver M. E. et al., 2014, ApJ, 782, 90
Coziol R., 2003, MNRAS, 344, 181
Cruzen S., Wehr T., Weistrop D., Angione R. J., Hoopes C., 2002, AJ, 123, 142
Cutri R. M. et al., 2012, Technical report, Explanatory Supplement to the WISE All-Sky Data Release Products.
Dekel A., Birnboim Y., 2006, MNRAS, 368, 2
Domínguez A. et al., 2013, ApJ, 763, 145
Driver S. P. et al., 2011, MNRAS, 413, 971
Elyiv A. A., Karachentsev I. D., Karachentseva V. E., Melnyk O. V., Makarov D. I., 2013, Astrophys. Bull., 68, 1
Gavazzi G., Boselli A., Cortese L., Arosio I., Gallazzi A., Pedotti P., Carrasco L., 2006, A&A, 446, 839
Gavazzi G., Fumagalli M., Galardo V., Grossetti F., Boselli A., Giovanelli R., Haynes M. P., Fabello S., 2012, A&A, 545, A16
Gavazzi G., Fumagalli M., Fossati M., Galardo V., Grossetti F., Boselli A., Giovanelli R., Haynes M. P., 2013, A&A, 553, A89
Grogin N. A., Geller M. J., 1999, AJ, 118, 2561
Grogin N. A., Geller M. J., 2000, AJ, 119, 32
Hoeft M., Gottlöber S., 2010, Adv. Astron., 2010
Hoyle F., Vogeley M. S., 2002, ApJ, 566, 641
Hoyle F., Vogeley M. S., Pan D., 2012, MNRAS, 426, 3041
Jarrett T. H. et al., 2011, ApJ, 735, 112
Jarrett T. H. et al., 2013, AJ, 145, 6
Johnson B. D. et al., 2007, ApJS, 173, 377
Jones M. G., Papastergis E., Haynes M. P., Giovanelli R., 2016, MNRAS, preprint (astro-ph/1510.07050)
Karachentsev I. D., Kaisin S. S., 2010, AJ, 140, 1241
Karachentsev I. D., Kaisina E. I., 2013, AJ, 146, 46
Karachentsev I. D., Makarov D. I., Kaisina E. I., 2013, AJ, 145, 101
Karachentseva V. E., Karachentsev I. D., Richter G. M., 1999, A&AS, 135, 221
Kauffmann G. et al., 2003, MNRAS, 341, 33
Kauffmann G., White S. D. M., Heckman T. M., Ménard B., Brinchmann J., Charlot S., Tremonti C., Brinkmann J., 2004, MNRAS, 353, 713
Kennicutt R. C., Jr, 1998, ApJ, 498, 541
Kennicutt R. C., Evans N. J., 2012, ARA&A, 50, 531
Kennicutt R. C., Jr, Lee J. C., Funes José G. S. J., Sakai S., Akiyama S., 2008, ApJS, 178, 247
Kereš D., Katz N., Weinberg D. H., Davé R., 2005, MNRAS, 363, 2
Kreckel K. et al., 2011, AJ, 141, 4
Kreckel K., Platen E., Aragón-Calvo M. A., van Gorkom J. H., van de Weygaert R., van der Hulst J. M., Beygu B., 2012, AJ, 144, 16
Kreckel K. et al., 2013, ApJ, 771, 62
Kron G. E., 1980, Ric. Astron., 10, 3
Kuhn B., Hopp U., Elsaesser H., 1997, A&A, 318, 405
Lee J. C., Kennicutt R. C., Jr, Funes S. J. J. G., Sakai S., Akiyama S., 2009a, ApJ, 692, 1305
Lee J. C. et al., 2009b, ApJ, 706, 599
Lee J. C. et al., 2011, ApJS, 192, 6
Lee J. C., Hwang H. S., Ko J., 2013, ApJ, 774, 62
Massey P., Strobel K., Barnes J. V., Anderson E., 1988, ApJ, 328, 315
Meidt S. E. et al., 2014, ApJ, 788, 144
Meurer G. R. et al., 2009, ApJ, 695, 765
Moorman C. M., Vogeley M. S., Hoyle F., Pan D. C., Haynes M. P., Giovanelli R., 2014, MNRAS, 444, 3559
Moorman C. M., Vogeley M. S., Hoyle F., Pan D. C., Haynes M. P., Giovanelli R., 2015, ApJ, 810, 108
Moorman C. M., Moreno J., White A., Vogeley M. S., Hoyle F., Giovanelli R., Haynes M. P., 2016, preprint (arXiv:1601.04092)
Oke J. B., 1990, AJ, 99, 1621
Patiri S. G., Betancort-Rijo J. E., Prada F., Klypin A., Gottlöber S., 2006a, MNRAS, 369, 335
Patiri S. G., Prada F., Holtzman J., Klypin A., Betancort-Rijo J., 2006b, MNRAS, 372, 1710
Peebles P. J. E., 2001, ApJ, 557, 495
Peimbert M., Torres-Peimbert S., 1992, A&A, 253, 349
Penny S. J. et al., 2015, MNRAS, 453, 3519
Petrosian V., 1976, ApJ, 209, L1
Platen E., van de Weygaert R., Jones B. J. T., 2007, MNRAS, 380, 551
Popescu C. C., Hopp U., Elsaesser H., 1997, A&A, 325, 881
Querejeta M. et al., 2015, ApJS, 219, 5
Raimann D., Storchi-Bergmann T., Bica E., Melnick J., Schmitt H., 2000, MNRAS, 316, 559
Ricciardelli E., Cava A., Varela J., Quilis V., 2014, MNRAS, 445, 4045
Rieder S., van de Weygaert R., Cautun M., Beygu B., Portegies Zwart S., 2013, MNRAS, 435, 222
Rieke G. H., Alonso-Herrero A., Weiner B. J., Pérez-González P. G., Blaylock M., Donley J. L., Marcillac D., 2009, ApJ, 692, 556
Rojas R. R., Vogeley M. S., Hoyle F., Brinkmann J., 2004, ApJ, 617, 50
Rojas R. R., Vogeley M. S., Hoyle F., Brinkmann J., 2005, ApJ, 624, 571
Salim S. et al., 2007, ApJS, 173, 267
Sánchez-Gallego J. R., Knapen J. H., Wilson C. D., Barmby P., Azimlu M., Courteau S., 2012, MNRAS, 422, 3208
Sarzi M. et al., 2006, MNRAS, 366, 1151
Schaap W. E., van de Weygaert R., 2000, A&A, 363, L29
Schiminovich D. et al., 2010, MNRAS, 408, 919
Schlegel D. J., Finkbeiner D. P., Davis M., 1998, ApJ, 500, 525
Sheth K. et al., 2010, PASP, 122, 1397
Stanonik K., Platen E., Aragón-Calvo M. A., van Gorkom J. H., van de Weygaert R., van der Hulst J. M., Peebles P. J. E., 2009, ApJ, 696, L6
Stern D. et al., 2012, ApJ, 753, 30
Sullivan M., Treyer M. A., Ellis R. S., Bridges T. J., Milliard B., Donas J., 2000, MNRAS, 312, 442
Szomoru A., van Gorkom J. H., Gregg M. D., 1996a, AJ, 111, 2141
Szomoru A., van Gorkom J. H., Gregg M. D., Strauss M. A., 1996b, AJ, 111, 2150
Terlevich R., Melnick J., Masegosa J., Moles M., Copetti M. V. F., 1991, A&AS, 91, 285
Tikhonov A. V., Karachentsev I. D., 2006, ApJ, 653, 969
Tremonti C. A. et al., 2004, ApJ, 613, 898
van de Weygaert R., Platen E., 2011, Int. J. Mod. Phys. Conf. Ser., 1, 41
van de Weygaert R., Schaap W., 2009, in Martínez V. J., Saar E., Martínez-González E., Pons-Bordería M.-J., eds, Lecture Notes in Physics, Vol. 665, Data Analysis in Cosmology. Springer-Verlag, Berlin, p. 291
van de Weygaert R. et al., 2011, in Ferreras I., Pasquali A., eds, The Void Galaxy Survey, Environment and the Formation of Galaxies: 30 Years Later. p. 17
Wegner G., Grogin N. A., 2008, AJ, 136, 1
Weistrop D., Hintzen P., Liu C., Lowenthal J., Cheng K.-P., Oliversen R., Brown L., Woodgate B., 1995, AJ, 109, 981
Wilson C. D. et al., 2009, ApJ, 693, 1736
Wright E. L. et al., 2010, AJ, 140, 1868
Wyder T. K. et al., 2007, ApJS, 173, 293

This paper has been typeset from a TEX/LATEX file prepared by the author.